*J. Fluid Mech.* (2019), *vol.* 866, *pp.* 316–349.  
doi:10.1017/jfm.2019.87

# Acoustic oscillations driven by boundary mass exchange

**Avshalom Offner[1,2], Rui Yang[2], Daniel Felman[2,3], Nimrod Elkayam[1,2], Yehuda Agnon[1,2,3,4] and Guy Z. Ramon[1,2,3,†]**

[1]The Nancy and Stephen Grand Technion Energy Programme, Technion – Israel Institute of Technology, Haifa 32000, Israel

[2]Department of Civil and Environmental Engineering, Technion – Israel Institute of Technology, Haifa 32000, Israel

[3]The Applied Mathematics Interdisciplinary Graduate Programme, Technion – Israel Institute of Technology, Haifa 32000, Israel

[4]Millstone/St. Louis Chair in Civil/Environmental Engineering, Technion – Israel Institute of Technology, Haifa 32000, Israel

(Received 22 May 2018; revised 18 January 2019; accepted 24 January 2019)

Thermoacoustic instability – self-sustained pressure oscillations triggered by temperature gradients – has become an increasingly studied topic in the context of energy conversion. Generally, the process relies on conductive heat transfer between a solid and the fluid in which the generated pressure oscillations are sustained. In the present study, the thermoacoustic theory is extended to include mass transfer; specifically, the working fluid is modified so as to incorporate a 'reactive' gas, able to exchange phase with a solid/liquid boundary through a sorption process (or through evaporation/condensation), such that most heat is transferred in the form of latent heat rather than through conduction. A set of differential equations is derived, accounting for phase-exchange heat and mass transfer, and de-coupled via a small-amplitude asymptotic expansion. These equations are solved and subsequently manipulated into the form of a wave equation, representing the small perturbation on the pressure field, and used to derive expressions for the time-averaged, second-order heat and mass fluxes. A stability analysis is performed on the wave equation, from which the marginal stability curve is calculated in terms of the temperature difference, $\Delta T_{onset}$, required for initiation of self-sustained oscillations. Calculated stability curves are compared with published experimental results, showing good agreement. Effects of gas mixture composition are studied, indicating that a lower heat capacity of the inert component, combined with a low boiling temperature and high latent heat of the reactive component substantially lower $\Delta T_{onset}$. Furthermore, an increase in the average mole fraction of the reactive gas, $C_m$ strongly affects onset conditions, leading to $\Delta T_{onset} \sim 5\,^{\circ}\mathrm{C}$ at the highest value of $C_m$ achievable under atmospheric pressure. An analysis of the system limit cycle is performed for a wide range of parameters, indicating a systematic decrease in the temperature difference capable of sustaining the limit cycle, as well as a significant distortion of the acoustic wave form as the phase-exchange mechanism becomes dominant. These findings, combined, reveal the underlying mechanisms by which a phase-exchange engine may produce

† Email address for correspondence: ramong@technion.ac.il

more acoustic power than its counterpart 'classical' thermoacoustic system, while its temperature difference is substantially lower.

**Key words:** phase change, instability

## 1. Introduction

Thermoacoustic interactions may generally be classified as processes involving conversions of heat to acoustic power (and *vice versa*). Over the past several decades, most studies of thermoacoustic phenomena are concerned with suppression of undesired acoustic waves produced spontaneously in combustion chambers due to the presence of large temperature gradients (Keller 1995; Fleifil *et al.* 1996; Dowling & Morgans 2005). However, the deliberate excitation of this instability by imposed temperature differences, to controllably generate self-sustained acoustic oscillations presents a growing application in the context of energy production. In this process, self-sustained oscillatory motion, accompanied by compression and expansion, generates heat transfer between the gas and a solid medium. Enhancing this effect is achieved by using a matrix of narrow channels, namely a 'stack', which increases the solid–gas contact area. While evidence of such devices dates back to the 19th century (Sondhauss 1850; Rijke 1859), a theoretical model, quantitatively capturing the phenomenon, was derived only a century later by Rott (1969), who formulated the linear theory of thermoacoustics, and later refined by Swift (1988). Swift (2002) extended this formulation to account for different geometric configurations, amongst which are looped-tube systems, first proposed by Ceperley (1979) and successfully demonstrated by Yazaki *et al.* (1998), in which the thermodynamic cycle resembles that of Stirling heat engines. Furthermore, Ward & Swift (1994) developed a highly flexible numerical tool for simulation of such systems, which is widely used by designers of thermoacoustic systems.

In the majority of reported studies on thermoacoustic devices, the working fluid is one (or more) of the noble gases or air. These inert gases are widely available and are non-hazardous when pressurised, making them suitable for operation at various working conditions. In such systems, heat is transferred between the solid and gas through conduction; accordingly, these are hereinafter referred to as conduction-driven thermoacoustic systems. However, a different approach may be taken by adding a condensable gas to the working fluid such that most heat is transferred through phase change, at constant temperature, rather than conduction. In this manner, mass is exchanged between the solid and gas mixture, and the temperature gradient imposed on the stack may be reduced, allowing a system to operate at lower temperature gradients. In their work on thermoacoustic refrigeration – exploiting acoustic power to pump heat up a temperature gradient – Hiller & Swift (2000) noticed condensation occurring in the cold side of the system, and concluded, using simplified models, that condensation occurred primarily on the stack walls. In a series of two papers, Raspet *et al.* (2002) and Slaton *et al.* (2002) derived the propagation equations of thermoacoustics for an air–water vapour mixture, accounting for evaporation/condensation at the stack walls, and calculated transport quantities such as acoustic power, as well as the heat and mass fluxes. Noda & Ueda (2013) constructed a simple system producing acoustic oscillations using a mixture of air and water (or ethanol) as the condensable fluid. They reported a dramatic decrease

in the temperature difference required for sustaining acoustic oscillations compared with a system employing dry air as the working fluid. A substantial decrease in the onset temperature difference was measured by Tsuda & Ueda (2015, 2017) for thermoacoustic systems employing an air–water vapour gas mixture, with the latter presenting experimental results of three different system geometries corresponding to standing wave, travelling wave and a combination of the two.

Tsuda & Ueda (2017) also measured the increase in pressure amplitude following onset of pressure oscillations in their systems. However, it appears that due to insufficient internal circulation of the finite volume of water in these closed systems, these oscillations could not maintain a limit cycle and naturally shut down shortly after the stability limit was exceeded. A similar standing-wave system with an air–water vapour gas mixture was recently reported by Meir, Offner & Ramon (2018), who demonstrated the first stable operation of a thermoacoustic engine with phase change. This engine was aligned vertically such that condensed water dripped back to the stack by gravity, creating a self-contained water circulation mechanism and successfully maintaining a stable limit cycle. At the reported heat inputs, however, this mechanism could not circulate the entire volume of water initially introduced to the system. As a result, a limit cycle was maintained with a hybrid stack consisting of 'dry' and 'wet' sections, each producing acoustic power through different heat transfer mechanisms. Meir *et al.* (2018) measured not only a dramatic decrease in the onset and limit cycle temperature differences (compared with the reference case of dry air as working gas), but also a significant increase in the produced pressure amplitude. While these studies have laid the foundations and illustrated the potential of this form of thermoacoustics, a systematic investigation of the physical mechanisms involved has yet to be performed.

In the present work, we generalise the theory of thermoacoustics with mass exchange between the solid and gas mixture, so as to account for any type of sorption process, for which phase change through evaporation/condensation is a limiting case. Configurations including any of these mechanisms are hereinafter referred to as phase-exchange thermoacoustic systems. The term 'phase exchange' captures all the above phenomena, noting that in sorption processes the sorbate does not change phase as in evaporation/condensation, but is absorbed (in the case of a gas–liquid system, e.g. ammonia/water) or adsorbed (in the case of a gas–solid system, e.g. water–vapour/silica) and subsequently desorbed from the sorbent material. The paper is organised as follows: § 2 is devoted to the derivation of the wave equation for linear phase-exchange thermoacoustics, subsequently used for the stability analysis as well as for calculations of the acoustic field, power and mass fluxes. In § 3 we describe the methods used for stability and limit cycle calculations, the results of which are presented and discussed in § 4, followed by concluding remarks in § 5.

## 2. Model formulation

We consider a 'stack' of length $L_s$ placed in a straight, closed cylindrical tube of length $L$ and diameter $d$, in which $d \ll L$ (see figure 1*a* for a schematic illustration). The stack is comprised of multiple layers of parallel plates, spaced $2h$ apart, as illustrated in figure 1(*b*).

The working fluid in the system is a binary gas mixture comprised of a 'reactive' gas, able to exchange phase with the stack plates, and an inert, non-reactive gas. The governing equations describing the flow in the tube and stack channels are (Landau & Lifshitz 1959)

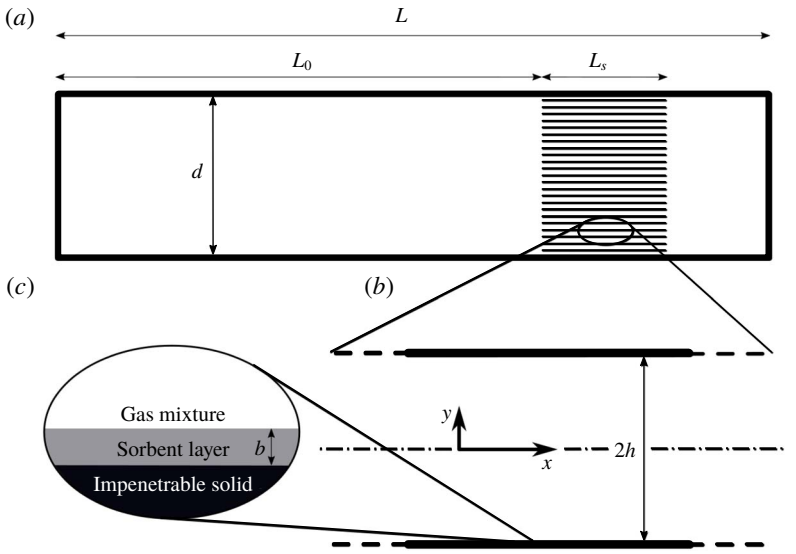


FIGURE 1. System schematic drawing: (*a*) a grid of narrow channels (stack) of length $L_s$ located at distance $L_0$ from a tube's closed end, (*b*) representative channel of parallel plates, $2h$ separated, aligned parallel to the tube axis and (*c*) a sorbent layer of thickness $b$ coating the solid impenetrable plates.

$$\frac{\mathcal{D}\rho}{\mathcal{D}t} = -\rho \nabla \cdot U, \tag{2.1}$$

$$\rho \frac{\mathcal{D}U}{\mathcal{D}t} = -\nabla p + \nabla \cdot \boldsymbol{\sigma}, \tag{2.2}$$

$$N \frac{\mathcal{D}C}{\mathcal{D}t} = -\nabla \cdot j, \tag{2.3}$$

$$\rho T \frac{\mathcal{D}s}{\mathcal{D}t} = \boldsymbol{\sigma} : \nabla U - \nabla \cdot (q - \mu_c j) - j \cdot \nabla \mu_c, \tag{2.4}$$

$$p = \frac{\rho R_g T}{M_{mix}}, \tag{2.5}$$

namely, the mixture continuity equation, Navier–Stokes equations, mass conservation of the reactive gas, the energy equation for a gas mixture and the equation of state for an ideal gas mixture. Here $\mathcal{D}/\mathcal{D}t$ is the two-dimensional material derivative operator, $\rho$ is the density, $t$ is time, $U \equiv \{u, v\}$ is the velocity vector comprised of the axial velocity, $u$, and $v$, the transverse velocity, $p$ is the pressure, $N$ is the molar density, $C \equiv N_r/N_{mix}$ is the reactive gas concentration, expressed as a mole fraction, with subscripts '$r$' and '$mix$' denoting the reactive gas component and the gas mixture, respectively, $s$ is the entropy, $\mu_c$ is the mixture chemical potential, $R_g$ is the universal gas constant, $T$ is the temperature and the mixture molar mass is defined as

$$M_{mix} = (M_r - M_i)C + M_i, \tag{2.6}$$

in which $M_r$ and $M_i$ are the molar masses of the reactive and inert gas components, respectively. The molar and heat fluxes are (Landau & Lifshitz 1959)

$$j = -ND \left[ \nabla C + \frac{k_T}{T} \nabla T + \frac{k_p}{p} \nabla p \right], \tag{2.7}$$

$$q = \left[ k_T \left( \frac{\partial \mu_c}{\partial C} \right)_{p,T} - T \left( \frac{\partial \mu_c}{\partial T} \right)_{p,C} + \mu_c \right] j - k \nabla T, \tag{2.8}$$

respectively, in which $D$ is the molecular diffusion coefficient, $k$ is the thermal conductivity and $k_T$ and $k_p$ are the thermal and baro-diffusion coefficients, respectively. The stress tensor is given by

$$\boldsymbol{\sigma} = \mu \boldsymbol{D} + \xi (\nabla \cdot U) \boldsymbol{I}, \tag{2.9}$$

where $\mu$ is the dynamic viscosity, $\boldsymbol{D} = \nabla U + (\nabla U)^{\mathrm{T}} - 2/3(\nabla \cdot U)\boldsymbol{I}$, $\xi$ is the volume viscosity and $\boldsymbol{I}$ is the identity matrix.

The temperature and pressure-driven diffusion coefficients, $k_T$ and $k_p$, are typically very small compared to the mass-diffusion term, as is the case considered herein, and are therefore set to zero, giving

$$j = -ND \nabla C, \tag{2.10}$$

$$q - \mu_c j = - \left[ T \left( \frac{\partial \mu_c}{\partial T} \right)_{p,C} j + k \nabla T \right]. \tag{2.11}$$

Using standard thermodynamic relations (Landau & Lifshitz 1959), we expand the entropy differential to obtain

$$\mathrm{d}s = \frac{c_p}{T} \mathrm{d}T - \frac{\beta}{\rho} \mathrm{d}p - \frac{1}{M_{mix}} \left( \frac{\partial \mu_c}{\partial T} \right)_{p,C} \mathrm{d}C, \tag{2.12}$$

where $c_p$ is the heat capacity at constant pressure, and $\beta$ is the thermal expansion coefficient. Considering an ideal gas mixture we write $\beta = 1/T$ and substitute (2.10)–(2.12) into (2.3) and (2.4) to obtain

$$N \frac{\mathcal{D}C}{\mathcal{D}t} = \nabla \cdot (ND \nabla C), \tag{2.13}$$

$$\begin{aligned} \rho c_p \frac{\mathcal{D}T}{\mathcal{D}t} - \frac{\mathcal{D}p}{\mathcal{D}t} + \frac{p}{R_g} \left( \frac{\partial \mu_c}{\partial T} \right)_{p,C} \frac{\mathcal{D}C}{\mathcal{D}t} \\ = \sigma : \nabla U + \nabla \cdot \left[ -\frac{pD}{R_g} \left( \frac{\partial \mu_c}{\partial T} \right)_{p,C} \nabla C + k \nabla T \right] + ND \nabla C \nabla \mu_c. \end{aligned} \tag{2.14}$$

Equations (2.1), (2.2), (2.13) and (2.14) represent a system of nonlinear, coupled partial differential equations. In what follows, we simplify these equations through a small-parameter asymptotic approximation.

### 2.1. *Long-wave theory approximation*

The geometry of the system under consideration (as shown in figure 1) satisfies $h \ll d \ll L$, allowing us to adopt a long-wave approximation in an attempt to simplify the governing equations. We begin by scaling the variables in the problem as follows

$$\left.\begin{aligned} x = \lambda \hat{x}; \quad y = h\hat{y}; \quad t = \omega^{-1}\hat{t}; \quad u = \omega\lambda\hat{u}; \quad v = \omega\lambda\hat{v}; \quad N = N_0\hat{N} \\ \rho = \rho_0\hat{\rho}; \quad p = \rho_0\omega^2\lambda^2\hat{p}; \quad T = \frac{\omega^2\lambda^2}{c_{p,0}}\hat{T}; \quad \mu_c = \frac{\omega^2\lambda^2 R_g}{c_{p,0}}\hat{\mu}_c, \\ \mu = \mu_0\hat{\mu}; \quad \xi = \xi_0\hat{\xi}; \quad D = D_0\hat{D}; \quad c_p = c_{p,0}\hat{c_p}; \quad k = k_0\hat{k}, \end{aligned}\right\} \tag{2.15}$$

where $\lambda = a/\omega$ is the wavelength with $a$ denoting the speed of sound and $\omega$ the angular frequency, subscripts '0' denote reference values for different quantities and the hat denotes a dimensionless quantity. We define the small parameter

$$\varepsilon = \frac{h}{\lambda} \ll 1, \tag{2.16}$$

and write the governing equations in their non-dimensional form, retaining quantities up to $O(\varepsilon)$ and discarding all hat signs for convenience,

$$\frac{\mathfrak{D}\rho}{\mathfrak{D}t} = -\rho\left(\varepsilon\frac{\partial u}{\partial x} + \frac{\partial v}{\partial y}\right), \tag{2.17}$$

$$\rho\frac{\mathfrak{D}u}{\mathfrak{D}t} = -\varepsilon\frac{\partial p}{\partial x} + \frac{\varepsilon}{\tau_{\nu_0}^2}\frac{\partial}{\partial y}\left(\mu\frac{\partial u}{\partial y}\right) + O(\varepsilon^2), \tag{2.18}$$

$$\rho\frac{\mathfrak{D}v}{\mathfrak{D}t} = -\frac{\partial p}{\partial y} + \frac{\varepsilon}{\tau_{\nu_0}^2}\frac{4}{3}\frac{\partial}{\partial y}\left(\mu\frac{\partial v}{\partial y}\right) + \frac{\varepsilon}{\tau_{\zeta_0}^2}\frac{\partial}{\partial y}\left(\xi\frac{\partial v}{\partial y}\right) + O(\varepsilon^2), \tag{2.19}$$

$$N\frac{\mathfrak{D}C}{\mathfrak{D}t} = \frac{\varepsilon}{\tau_{D_0}^2}\frac{\partial}{\partial y}\left(ND\frac{\partial C}{\partial y}\right) + O(\varepsilon^2), \tag{2.20}$$

$$\begin{aligned}
&\rho c_p\frac{\mathfrak{D}T}{\mathfrak{D}t} - \frac{\mathfrak{D}p}{\mathfrak{D}t} - p\left(\frac{\partial\mu_c}{\partial T}\right)_{p,C}\frac{\mathfrak{D}C}{\mathfrak{D}t} \\
&\quad= \varepsilon\left[\frac{\xi}{\tau_{\zeta_0}^2}\left(\frac{\partial v}{\partial y}\right)^2 + \frac{\mu}{\tau_{\nu_0}^2}\left(\left(\frac{\partial u}{\partial y}\right)^2 + \frac{4}{3}\left(\frac{\partial v}{\partial y}\right)^2\right)\right] - \frac{\varepsilon}{\tau_{D_0}^2}\frac{p}{N}\frac{\partial}{\partial y}\left[\left(\frac{\partial\mu_c}{\partial T}\right)_{p,C}ND\frac{\partial C}{\partial y}\right] \\
&\qquad- \frac{\varepsilon}{\tau_{D_0}^2}\frac{p}{T}D\frac{\partial C}{\partial y}\left[\left(\frac{\partial\mu_c}{\partial T}\right)_{p,C}\frac{\partial T}{\partial y} - \frac{\partial\mu_c}{\partial y}\right] + \frac{\varepsilon}{\tau_{\alpha_0}^2}\frac{\partial}{\partial y}\left(k\frac{\partial T}{\partial y}\right) + O(\varepsilon^2),
\end{aligned} \tag{2.21}$$

where

$$\frac{\mathfrak{D}}{\mathfrak{D}t} \equiv \varepsilon\left(\frac{\partial}{\partial t} + u\frac{\partial}{\partial x}\right) + v\frac{\partial}{\partial y} \tag{2.22}$$

is a dimensionless material derivative operator and

$$\tau_{n_0} \equiv h\sqrt{\frac{\omega}{n_0}}, \quad n = \nu, \zeta, \alpha, D, \tag{2.23}$$

is a dimensionless parameter representing the ratio of characteristic time scales of the acoustic oscillations and viscous, conductive and diffusive transport across the channel height, represented, respectively, by the gas properties as follows: $\nu_0 \equiv \mu_0/\rho_0$ for the kinematic viscosity, $\zeta_0 \equiv \xi_0/\rho_0$ for the kinematic volume viscosity, $\alpha_0 \equiv k_0/(\rho_0 c_{p,0})$ for the thermal diffusivity and $D_0$ for the molecular diffusion coefficient.

Next, we write all quantities as a series expansion of the form

$$g = g_m(x, y) + \varepsilon g_1(x, y, t) + O(\varepsilon^2), \tag{2.24}$$

in which the $O(1)$ term is given the subscript '$m$' (for mean) to highlight its correspondence to the quantity time-averaged value. Note that the zeroth-order, time-averaged velocities $u$ and $v$ are zero since the flow is purely oscillatory. We

substitute these expansions into (2.17)–(2.21), and write the equations to leading order. The continuity equation for the mixture (2.17), becomes

$$\frac{\partial}{\partial y}(\rho_m v_1) = 0, \tag{2.25}$$

such that $\rho_m v_1 = f(x, t)$. Symmetry dictates that the transverse velocity at the mid-plane between plates, $v(x, 0, t)$, is zero. Since $\rho_m \neq 0$, we have $v_1 = 0$ such that $v = \varepsilon^2 v_2(x, y, t) + O(\varepsilon^3)$. We note that since $v = O(\varepsilon^2)$, equations (2.18) and (2.20)–(2.21) are divided by $\varepsilon$ to formally retain $O(1)$ terms. Equations (2.18)–(2.19) become, simply,

$$\frac{\partial p_m}{\partial x} = \frac{\partial p_m}{\partial y} = 0, \tag{2.26}$$

stating that the pressure, to leading order, is constant. From (2.20) we obtain

$$\frac{\partial}{\partial y}\left(N_m D_m \frac{\partial C_m}{\partial y}\right) = 0, \tag{2.27}$$

such that $N_m D_m \partial C_m/\partial y = f(x, t)$. Symmetry requires that $\partial/\partial y|_{y=0} = 0$ is satisfied for all quantities, and since $N_m$, $D_m \neq 0$ we deduce that $\partial C_m/\partial y = 0$. Consequently, to leading order, equation (2.21) simplifies to

$$\frac{\partial}{\partial y}\left(k_m \frac{\partial T_m}{\partial y}\right) = 0. \tag{2.28}$$

Similar arguments lead to $\partial T_m/\partial y = 0$, noting that $k_m \neq 0$. The quantities $p_m$, $C_m$, and $T_m$ define the zeroth-order time-averaged thermodynamic state of the gas; as these are independent of $y$ it follows that

$$\frac{\partial g_m}{\partial y} = 0, \tag{2.29}$$

with $g$ denoting any of the quantities in the system.

At $O(\varepsilon)$, the expansion of (2.17)–(2.20) yields

$$\frac{\partial \rho_1}{\partial t} + u_1 \frac{\mathrm{d}\rho_m}{\mathrm{d}x} = -\rho_m \left(\frac{\partial u_1}{\partial x} + \frac{\partial v_2}{\partial y}\right), \tag{2.30}$$

$$\frac{\partial u_1}{\partial t} = -\frac{1}{\rho_m}\frac{\partial p_1}{\partial x} + \frac{1}{\tau_\nu^2}\frac{\partial^2 u_1}{\partial y^2}, \tag{2.31}$$

$$\frac{\partial p_1}{\partial y} = 0, \tag{2.32}$$

$$\frac{\partial C_1}{\partial t} + u_1 \frac{\mathrm{d}C_m}{\mathrm{d}x} = \frac{1}{\tau_D^2}\frac{\partial^2 C_1}{\partial y^2}, \tag{2.33}$$

where

$$\tau_n = h\sqrt{\frac{\omega}{n_m}}, \quad n = \nu, D, \alpha, \tag{2.34}$$

with $n$ denoting a dimensional quantity, dependent on $x$, differing from $n_0$ which corresponds to a reference value. Using (2.32), $O(\varepsilon)$ in (2.21) becomes

$$\frac{\partial T_1}{\partial t}+u_1\frac{\mathrm{d}T_m}{\mathrm{d}x}-\frac{1}{\rho_m c_{p,m}}\frac{\partial p_1}{\partial t}=\frac{1}{\tau_\alpha^2}\frac{\partial^2 T_1}{\partial y^2}+\frac{p_m}{\rho_m c_{p,m}}\left(\frac{\partial \mu_c}{\partial T}\right)_{p,C}\left[\frac{\partial C_1}{\partial t}+u_1\frac{\mathrm{d}C_m}{\mathrm{d}x}-\frac{1}{\tau_D^2}\frac{\partial^2 C_1}{\partial y^2}\right], \tag{2.35}$$

in which the terms in square brackets sum up to zero, according to (2.33). Finally, the $O(\varepsilon)$ energy equation reads

$$\frac{\partial T_1}{\partial t}+u_1\frac{\mathrm{d}T_m}{\mathrm{d}x}-\frac{1}{\rho_m c_{p,m}}\frac{\partial p_1}{\partial t}=\frac{1}{\tau_\alpha^2}\frac{\partial^2 T_1}{\partial y^2}. \tag{2.36}$$

As all governing equations, equations (2.30), (2.31), (2.33) and (2.36), contain only time-averaged terms of $\nu$, $\alpha$, $D$ and $c_p$, we hereinafter omit the subscript '$m$' in these quantities for convenience.

### 2.2. *Derivation of the wave equation*

The long-wave asymptotic analysis produced a set of simplified equations with all time-averaged quantities dependent only on the longitudinal coordinate $x$. Next, we follow Rott (1969) and eliminate time dependencies by assuming harmonic oscillations. Since $t$ is scaled with $\omega^{-1}$ all variables may be expanded as $g = g_m(x)+\varepsilon\mathrm{Re}[g_1(x,y)\mathrm{e}^{\mathrm{i}t}]$, where it is recalled that $g$ denotes any of the quantities in the system. Equations (2.31), (2.33) and (2.36) then take the form

$$\frac{\partial^2 u_1}{\partial y^2}-\hat{\tau}_\nu^2 u_1=\frac{\tau_\nu^2}{\rho_m}\frac{\mathrm{d}p_1}{\mathrm{d}x}, \tag{2.37}$$

$$\frac{\partial^2 T_1}{\partial y^2}-\hat{\tau}_\alpha^2 T_1=-\frac{\hat{\tau}_\alpha^2}{\rho_m c_p}p_1+\tau_\alpha^2 u_1\frac{\mathrm{d}T_m}{\mathrm{d}x}, \tag{2.38}$$

$$\frac{\partial^2 C_1}{\partial y^2}-\hat{\tau}_D^2 C_1=\tau_D^2 u_1\frac{\mathrm{d}C_m}{\mathrm{d}x}, \tag{2.39}$$

where $\hat{\tau}_n=\mathrm{i}^{1/2}\tau_n$. Solutions to (2.37)–(2.38) were derived by Swift (1988), yielding the velocity and temperature distributions

$$u_1(x,y)=\frac{\mathrm{i}H_\nu}{\rho_m}\frac{\mathrm{d}p_1}{\mathrm{d}x}, \tag{2.40}$$

$$T_1(x,y)=\frac{H_\alpha}{\rho_m c_p}p_1+\mathrm{i}\left[\frac{H_\alpha-PrH_\nu}{F_\nu(1-Pr)}\right]\frac{\mathrm{d}T_m}{\mathrm{d}x}\langle u_1\rangle, \tag{2.41}$$

in which $Pr$ is the Prandtl number and

$$H_n=1-\frac{\cosh(\hat{\tau}_n y)}{\cosh(\hat{\tau}_n)}, \tag{2.42}$$

$$F_n\equiv\int_0^1 H_n\,\mathrm{d}y=1-\frac{\tanh(\hat{\tau}_n)}{\hat{\tau}_n}, \tag{2.43}$$

$$\langle u_1\rangle\equiv\int_0^1 u_1\,\mathrm{d}y. \tag{2.44}$$

Solving (2.39) we note the boundary condition of symmetry at the mid-plane between plates, stating $\partial C_1/\partial y|_{y=0} = 0$, and the mass balance at the gas–sorbent interface (Weltsch *et al.* 2017)

$$\left.\frac{\partial C_1}{\partial y}\right|_{y=1} = -\frac{K\Lambda\hat{\tau}_D^2}{1+\hat{\tau}_k^2}\frac{N^s}{N_m}(1-C_m)\left(\frac{C_m p_1}{p_m} + C_1|_{y=1}\right), \tag{2.45}$$

in which the mass flux in the gas mixture, comprised of diffusion and a non-zero mixture velocity (Stefan flow), is equated to the mass flux entering/leaving the sorbent layer, expressed through a first-order sorption reaction. The sorbent layer thickness, $b$ (see figure 1*c*), is assumed to be very small (satisfying $\Lambda \equiv b/h \ll 1$, with $h$ denoting half the plate spacing) such that diffusion within the layer may be neglected and the reactive gas concentration within the sorbent cross-section is uniform. $K \equiv k_a/k_d$ is the equilibrium partition coefficient of the sorbent/sorbate system, with $k_a$ and $k_d$ denoting forward and backward reaction constants, respectively, $\hat{\tau}_k \equiv (\mathrm{i}\omega/k_d)^{1/2}$ is a ratio of oscillation to desorption kinetics time-scales and $N^s$ is the sorbent layer capacity for sorption of reactive gas moles per m$^3$. The distribution of $C_1$ is then

$$C_1(x,y) = -\frac{C_m(1-H_D)}{p_m\eta_D}p_1 + \mathrm{i}\left[\frac{1 - ScH_v - \dfrac{\eta_v}{\eta_D}(1-H_D)}{F_v(1-Sc)}\right]\frac{\mathrm{d}C_m}{\mathrm{d}x}\langle u_1\rangle, \tag{2.46}$$

in which $Sc$ is the Schmidt number and

$$\eta_n = 1 + \frac{1+\hat{\tau}_k^2}{K\Lambda}\frac{N_m}{N^s}\frac{1-F_n}{1-C_m}, \quad n = v, D \tag{2.47}$$

is a parameter describing sorption kinetics. In the case of evaporation/condensation from/to a thin film, the value of $N^s$ is not constrained since the liquid has infinite capacity for condensed vapour. Accordingly, $N^s_{(Evap.)} \to \infty$ such that $\eta_{n(Evap.)} \to 1$, and

$$C_{1(Evap.)}(x,y) = -\frac{C_m}{p_m}(1-H_D)p_1 + \mathrm{i}\left[\frac{H_D - ScH_v}{F_v(1-Sc)}\right]\frac{\mathrm{d}C_m}{\mathrm{d}x}\langle u_1\rangle. \tag{2.48}$$

The same result is reproduced for the limit of an 'ideal' sorption process, in which $K \to \infty$.

The $O(\varepsilon)$ continuity equation, eliminating time derivatives, is

$$\mathrm{i}\rho_1 + u_1\frac{\mathrm{d}\rho_m}{\mathrm{d}x} + \rho_m\left(\frac{\partial u_1}{\partial x} + \frac{\partial v_2}{\partial y}\right) = 0. \tag{2.49}$$

The terms $\rho_1$ and $\mathrm{d}\rho_m/\mathrm{d}x$ are derived through the total differential of the density, calculated according to (2.5)

$$\mathrm{d}\rho = \frac{\partial\rho}{\partial p}\mathrm{d}p + \frac{\partial\rho}{\partial T}\mathrm{d}T + \frac{\partial\rho}{\partial C}\mathrm{d}C = \rho\left(\frac{\mathrm{d}p}{p} - \frac{\mathrm{d}T}{T} + \frac{\varphi\,\mathrm{d}C}{1+\varphi C}\right) \tag{2.50}$$

in which

$$\varphi = \frac{M_r - M_i}{M_i} \tag{2.51}$$

is a parameter containing information about the molecular masses of the two components in the mixture. The term $1+\varphi C$ in the denominator cannot be zero since $-1<\varphi$ and $0\leqslant C\leqslant 1$. Substituting these terms into the continuity equation, we take a cross-sectional average of (2.49), according to the definition in (2.44), to obtain

$$\mathrm{i}\left(\frac{p_1}{p_m}-\frac{\langle T_1\rangle}{T_m}+\frac{\varphi\langle C_1\rangle}{1+\varphi C_m}\right)+\langle u_1\rangle\left(-\frac{1}{T_m}\frac{\mathrm{d}T_m}{\mathrm{d}x}+\frac{\varphi}{1+\varphi C_m}\frac{\mathrm{d}C_m}{\mathrm{d}x}\right)+\frac{\partial\langle u_1\rangle}{\partial x}+v_2|_{y=1}=0. \tag{2.52}$$

The term $v_2|_{y=1}$ is the result of the cross-sectional average

$$\left\langle\frac{\partial v_2}{\partial y}\right\rangle\equiv\int_0^1\frac{\partial v_2}{\partial y}\mathrm{d}y=v_2|_{y=1}-v_2|_{y=0}, \tag{2.53}$$

where the transverse velocity at the mid-plane between the solid plates, $v_2|_{y=0}$, is zero due to symmetry. The mixture velocity is given by

$$v_2=\frac{\rho_{m(r)}v_{2(r)}+\rho_{m(i)}v_{2(i)}}{\rho_m}, \tag{2.54}$$

with the subscripts $r$ and $i$ denoting reactive and inert gas components, respectively. The relative velocity between components in a binary mixture is derived using Fick's law (Bird, Stewart & Lightfoot 2007), and in our scaled form is given by

$$v_{2(r)}-v_{2(i)}=-\frac{1}{C_m(1-C_m)\tau_D^2}\frac{\partial C_1}{\partial y}. \tag{2.55}$$

The no-penetration condition for the inert gas at the interface states $v_{2(i)}=0$, such that

$$v_2=\frac{\rho_{m(r)}}{\rho_m}v_{2(r)}=\frac{C_m(1+\varphi)}{1+\varphi C_m}v_{2(r)}, \tag{2.56}$$

eventually resulting in

$$v_2|_{y=1}=-\frac{(1+\varphi)}{(1+\varphi C_m)(1-C_m)\tau_D^2}\left.\frac{\partial C_1}{\partial y}\right|_{y=1}. \tag{2.57}$$

Substituting (2.40), (2.41), (2.46), and (2.57) into (2.52) we finally obtain the wave equation

$$\frac{\mathrm{d}}{\mathrm{d}x}\left(\frac{F_v}{\rho_m}\frac{\mathrm{d}p_1}{\mathrm{d}x}\right)+A\frac{\mathrm{d}p_1}{\mathrm{d}x}+B^2p_1=0, \tag{2.58}$$

where

$$A=\frac{1}{\rho_m}\left[\frac{F_\alpha-F_v}{1-Pr}\frac{1}{T_m}\frac{\mathrm{d}T_m}{\mathrm{d}x}+\frac{1-F_v-\dfrac{\eta_v}{\eta_D}(1-F_D)}{1-Sc}\frac{1}{1-C_m}\frac{\mathrm{d}C_m}{\mathrm{d}x}\right], \tag{2.59}$$

$$B^2=\frac{1}{p_m}\left(1-\frac{\gamma-1}{\gamma}F_\alpha+\frac{C_m}{1-C_m}\frac{1-F_D}{\eta_D}\right). \tag{2.60}$$

In the limit $\eta_n\to 1$, representing phase change through evaporation/condensation, equation (2.58) recovers the result of Raspet *et al.* (2002), while for $C_m=\mathrm{d}C_m/\mathrm{d}x=0$ it recovers that of Rott (1969).

### 2.3. *Time-averaged heat and mass fluxes*

In what follows, we derive the heat and mass fluxes in an acoustic field, comprised of diffusion and acoustic 'streaming' – second-order, time-averaged transport quantities of the form $\overline{u_1 g_1} = 1/2\,\mathrm{Re}[\langle \widetilde{u_1} g_1 \rangle]$, where $g$ may be any scalar quantity. We first write the reactive gas mass flux and the total power flux in their dimensional form

$$\dot{m} = M_r N_m \left( \frac{1}{2}\mathrm{Re}[\langle \widetilde{u_1} C_1 \rangle] - D\frac{\mathrm{d}C_m}{\mathrm{d}x} \right), \tag{2.61}$$

$$\dot{H} = \rho_m c_p \left( \frac{1}{2}\mathrm{Re}[\langle \widetilde{u_1} T_1 \rangle] - \alpha \frac{\mathrm{d}T_m}{\mathrm{d}x} \right) + \dot{m} l_h, \tag{2.62}$$

where $l_h$ is the reactive fluid's heat of evaporation/sorption. The term $\dot{m} l_h$ in (2.62) is the heat flux carried by the oscillating reactive gas that exchanges mass with the boundary. In scaled form, we have

$$l_h = \lambda^2 \omega^2 \widehat{l_h}, \quad \dot{m} = \varepsilon^2 M_r N_0 \lambda \omega \hat{\dot{m}}, \quad \dot{H} = \varepsilon^2 \rho_0 \lambda^3 \omega^3 \hat{\dot{H}}, \tag{2.63a–c}$$

where the mass and total power fluxes are second-order streaming effects, and are hence scaled with $\varepsilon^2$. The mass flux derivation appears in Weltsch *et al.* (2017), and in our scaled form it reads

$$\begin{aligned} \dot{m} \;=\; & N_m \left\{ \frac{C_m}{2p_m(1+Sc)} \mathrm{Re}\left[ \frac{\widetilde{p_1} u_1}{\eta_D} \left( \frac{F_D - \widetilde{F_v}}{\widetilde{F_v}} \right) \right] \right. \\ & \left. - \frac{|u_1|^2}{2(1-Sc^2)|F_v|^2} \mathrm{Im}\left[ \widetilde{F_v}(1+Sc) - \frac{\eta_v}{\eta_D}(\widetilde{F_v} - F_D) \right] \frac{\mathrm{d}C_m}{\mathrm{d}x} - \frac{1}{\tau_D^2}\frac{\mathrm{d}C_m}{\mathrm{d}x} \right\}, \end{aligned} \tag{2.64}$$

where, hereinafter, the velocity $u_1$ refers to the cross-sectionally averaged velocity, defined in (2.44), discarding the angle brackets for convenience. Using (2.64) we write the total power flux in a phase-exchange system

$$\begin{aligned} \dot{H} = & \frac{1}{2}\left( \frac{1}{1+Pr}\mathrm{Re}\left[ \widetilde{p_1} u_1 \left( \frac{F_\alpha + Pr\widetilde{F_v}}{\widetilde{F_v}} \right) \right] + \frac{C_m \widehat{M} N_m l_h}{p_m} \frac{1}{1+Sc} \mathrm{Re}\left[ \frac{\widetilde{p_1} u_1}{\eta_D} \left( \frac{F_D - \widetilde{F_v}}{\widetilde{F_v}} \right) \right] \right) \\ & - \frac{|u_1|^2}{2|F_v|^2} \left( \frac{\rho_m c_p}{1-Pr^2} \mathrm{Im}[F_\alpha + Pr\widetilde{F_v}] \frac{\mathrm{d}T_m}{\mathrm{d}x} + \frac{\widehat{M} N_m l_h}{1-Sc^2} \mathrm{Im}\left[ \widetilde{F_v}(1+Sc) - \frac{\eta_v}{\eta_D}(\widetilde{F_v} - F_D) \right] \frac{\mathrm{d}C_m}{\mathrm{d}x} \right) \\ & - \left( \frac{\rho_m c_p}{\tau_\alpha^2} \frac{\mathrm{d}T_m}{\mathrm{d}x} + \frac{\widehat{M} N_m l_h}{\tau_D^2} \frac{\mathrm{d}C_m}{\mathrm{d}x} \right), \end{aligned} \tag{2.65}$$

where $\widehat{M} \equiv M_r / M_{mix,0}$ is a ratio of molar masses, with $M_{mix,0}$ denoting a reference value for the mixture molar mass.

## 3. Solution methodology

The methods used to solve the equations describing the system stability limit and limit cycle, along with the simplifying assumptions made, are detailed and discussed below. Our analysis of a phase-exchange thermoacoustic system requires an additional definition of $C_m$, the reactive gas time-averaged concentration (mole fraction) in

the mixture. Considering equilibrium between the sorption layer and gas mixture phases (far from saturation of the sorbent), $C_m$ must be linked with the temperature, at a given pressure. Here, the Clausius–Clapeyron relation is used, leading to

$$C_m = \exp\left[-\frac{l_h}{R}\left(\frac{1}{T_m} - \frac{1}{T_{max}}\right)\right], \tag{3.1}$$

where $R = R_g/M_r$ is the reactive component specific gas constant, $T_m$ is the mean temperature and $T_{max}$ is the temperature at which $C_m = 1$. The concentration gradient is then linked with the temperature gradient via

$$\frac{\mathrm{d}C_m}{\mathrm{d}x} = \frac{\mathrm{d}C_m}{\mathrm{d}T_m}\frac{\mathrm{d}T_m}{\mathrm{d}x} = \frac{l_h}{R}\frac{C_m}{T_m^2}\frac{\mathrm{d}T_m}{\mathrm{d}x}. \tag{3.2}$$

### 3.1. *Stability analysis*

In a thermoacoustic engine converting heat into acoustic power, one side of the stack is heated (the right side in figure 1*a*) while the other side is maintained at a lower temperature (the ambient, if possible). The increasing temperature gradient imposed on the stack produces acoustic power which, at first, is fully dissipated in the stack and the empty segments of the tube. The stability limit may be defined as the point at which the produced and dissipated power is exactly balanced, such that oscillations are not augmented nor decayed. At this state, a small perturbation will trigger the instability, giving rise to a growth in the amplitude of the pressure oscillations. In what follows, we seek the temperature difference $\Delta T_{onset}$, between the two sides of the stack, sufficient for onset of the instability to occur in the system. The mean temperature profile, $T_m(x)$, is generally unknown. In the empty segments of the tube it is assumed that the temperature is constant, while along the stack a temperature gradient is imposed on the solid and gas. The stack cold-side temperature, $T_c$, is assumed to be a prescribed constant. In the stable state, heat is transferred across the stack via conduction. Assuming the heating rate is sufficiently low, the temperature profile is the solution to a one-dimensional, steady-state heat equation, such that $\mathrm{d}T_m/\mathrm{d}x = \Delta T/L_s$, with $L_s$ denoting the stack length. The wave equation, equation (2.58), is then a linear, homogeneous ordinary differential equation. The stability limit is sought by targeting the non-trivial solution satisfying the eigenvalue problem. We present two different methods for solving this problem: the first is a numerical scheme, while the second is a semi-analytic, simple approach involving acoustic power calculations.

#### 3.1.1. *Finite differences scheme*

In this numerical scheme we approximate pressure and velocity derivatives using finite differences, obtaining a linear, homogeneous set of equations. We begin by writing (2.58) as two first-order ordinary differential equations (ODEs) for the pressure and velocity oscillations

$$\frac{\mathrm{d}p_1}{\mathrm{d}x} = -\frac{\mathrm{i}\rho_m}{F_v}u_1, \tag{3.3}$$

$$\frac{\mathrm{d}u_1}{\mathrm{d}x} = -\mathrm{i}B^2 p_1 - \frac{A}{F_v}u_1, \tag{3.4}$$

where $A$ and $B$ are defined in (2.59)–(2.60). In order to solve the system of equations, the tube is divided into $n$ equally spaced intervals, each interval $\Delta x = L/n$ long. The

derivatives $\mathrm{d}p_1/\mathrm{d}x$ and $\mathrm{d}u_1/\mathrm{d}x$ are expressed using forward differences, such that (3.3) and (3.4) are translated into $2n$ equations. The remaining 2 equations arise from boundary conditions, demanding $u_{1,1} = u_{1,n+1} = 0$, namely that the velocity is zero at the closed ends. Ultimately, the following system is obtained

$$\boldsymbol{A} \begin{pmatrix} p_{1,1} \\ \vdots \\ p_{1,n+1} \\ u_{1,1} \\ \vdots \\ u_{1,n+1} \end{pmatrix} = 0, \tag{3.5}$$

where $\boldsymbol{A}$ is the coefficients matrix, and the vector comprises pressure and velocity at all the discrete points in the system. We seek the non-trivial solution by setting $\det(\boldsymbol{A}) = 0$. Since $\boldsymbol{A} \in \mathbb{C}$, guesses for two variables in $\boldsymbol{A}$ are required to allow the use of a gradient-based method, targeting $\mathrm{Re}[\det(\boldsymbol{A})] = \mathrm{Im}[\det(\boldsymbol{A})] = 0$. Our guesses are the resonant frequency, $\omega$, and the temperature difference on the stack, $\Delta T$. The value of $n$, arbitrarily chosen to increase calculation accuracy, determines the number of eigenvalues in $\boldsymbol{A}$, representing different harmonic modes. As our model assumes a monochromatic wave, neglecting effects of higher harmonics, we are only interested in the smallest eigenvalue of $\boldsymbol{A}$, corresponding to the resonant frequency of the first natural mode, $\omega$.

3.1.2. *Zero acoustic power – standing-wave approximation*

In this approach, we follow Arnott *et al.* (1994) and make the argument that the total acoustic power within the system – produced and dissipated – sums up to zero under onset conditions. In this stability limit, any increase in $\mathrm{d}T_m/\mathrm{d}x$ will enhance the oscillations.

In a low aspect-ratio straight tube, oscillations only slightly deviate from a standing-wave form, where pressure and velocity are 90° out of phase. If the Helmholtz number, $\Omega$, satisfies

$$\Omega = \frac{\omega L_s}{a} \ll 1, \tag{3.6}$$

the stack is very short compared with the wavelength, allowing us to assume the wave form is only weakly distorted by the presence of the stack. Accordingly, we may use the standing-wave approximation (Swift 1988) for the pressure and velocity perturbations

$$p_1 = p_A \cos(x/\lambda), \tag{3.7}$$

$$u_1 = \frac{\mathrm{i}p_A}{\rho_m a} \sin(x/\lambda), \tag{3.8}$$

where $p_A$ is the (dimensional) maximum pressure amplitude. We use (2.15) to scale these equations, approximating $\rho_m$ and $a$ as their reference values ($\rho_0$ and $\lambda\omega$, respectively) for simplicity, to obtain

$$p_1 = p_A \cos(x), \tag{3.9}$$

$$u_1 = \mathrm{i}p_A \sin(x), \tag{3.10}$$

where $p_A$ is the scaled maximum pressure amplitude.

The time-averaged acoustic power flux is

$$\dot{W} = \frac{1}{2\pi}\int_0^{2\pi} p_1(x,t)u_1(x,t)\,\mathrm{d}t = \frac{1}{2}\mathrm{Re}[\widetilde{p}_1 u_1], \tag{3.11}$$

where the tilde denotes a complex conjugate. Substituting (3.9) and (3.10) into (3.11) yields the expected result $\dot{W}=0$, reproducing a well-known attribute of pure standing waves producing zero acoustic power. Seeking a non-trivial result, we take the derivative of (3.11) to obtain

$$\frac{\mathrm{d}\dot{W}}{\mathrm{d}x} = \frac{1}{2}\mathrm{Re}\left[\widetilde{u}_1\frac{\mathrm{d}p_1}{\mathrm{d}x} + \widetilde{p}_1\frac{\mathrm{d}u_1}{\mathrm{d}x}\right], \tag{3.12}$$

into which (3.3) and (3.4) are substituted and only then the standing-wave pressure and velocity distributions may be used. This way the imperfect phasing between pressure and velocity is accounted for in the differential relations of (3.3) and (3.4). Ultimately we obtain

$$\frac{\mathrm{d}\dot{W}}{\mathrm{d}x} = \frac{p_A^2}{2}\left(\rho_m \mathrm{Im}\left[\frac{1}{F_\nu}\right]\sin^2(x) + \mathrm{Im}[B^2]\cos^2(x) - \frac{\rho_m}{2}\mathrm{Im}\left[\frac{A}{F_\nu}\right]\sin(2x)\right), \tag{3.13}$$

which may be integrated over all the segments in the system and equated to zero, resulting in an implicit equation for $\Delta T$ on the stack. The numerical solution to this equation is the desired temperature difference $\Delta T_{onset}$. Since $\Delta T_{onset}$ is not large, the gas properties do not vary significantly with temperature. For simplicity, all quantities besides $C_m$ are taken as constants, representative of the working fluid mixture and independent of $T_m$.

### 3.2. *Limit cycle analysis*

Following the loss of stability, the oscillations in a system grow until, given sufficient time, the oscillation amplitude saturates, marking a system limit cycle. In our case, equations (3.3)–(3.4), and (2.65) define a boundary value problem of three coupled, nonlinear ODEs, the solution of which, for $p_1(x)$, $u_1(x)$ and $T_m(x)$, marks the system's limit cycle. Equation (2.65) is manipulated into the form $\mathrm{d}T_m/\mathrm{d}x = f(p1, u1, T_m, \dot{H})$; as in § 3.1, the temperature is assumed to remain constant in the empty duct segments, while in the stack the total power flux, $\dot{H}$, is constant and, to a good degree of accuracy, represents the heat flux input to the system – a parameter of our choice – allowing us to assume $\dot{H} \approx Q_h$ and avoid an additional differential equation for $\dot{H}$ (Swift 2002). We use a fourth-order Runge–Kutta method to solve the initial value problem, targeting (as in § 3.1) the no-penetration condition at the closed end, $\mathrm{Re}[u_1(x=L)] = \mathrm{Im}[u_1(x=L)] = 0$, and initially guessing $\omega$ and the initial pressure amplitude $p_1(x=0)$.

## 4. Results and discussion

### 4.1. *Stability analysis*

In this section we present stability curves, in which the region beneath and above a curve represents the stable and unstable states, respectively. The values on a curve represent the minimum temperature difference, imposed on the stack, required to trigger an instability in the system. All results are calculated at a mean pressure $p_m = 1$ bar. Unless otherwise stated, results are calculated for $\eta_\nu = \eta_D = 1$, standing for ideal sorption processes or for evaporation/condensation (see § 2.2).

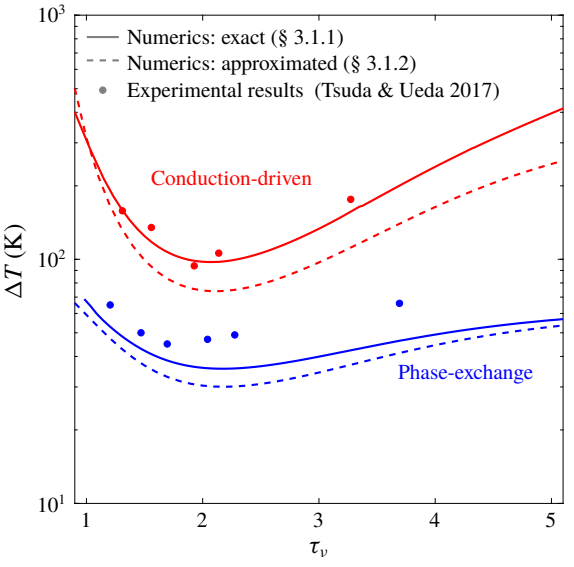


FIGURE 2. (Colour online) Stability curves for conduction-driven (red) and phase-exchange (blue) thermoacoustic systems, in which the working fluid is air or an air–water mixture, respectively, shown as a function of the Womersley number, $\tau_v$. Solid and dashed curves are calculated using the approaches described in § 3.1. All calculations assume ideal sorption ($\eta_v = \eta_D = 1$). The mean pressure is $p_m = 1$ bar, the stack cold-side temperature is $T_c = 23\,^{\circ}\mathrm{C}$, and scaled stack length and location are $L_s/L = 0.026$ and $L_0/L = 0.84$, respectively. Experimental results, marked by filled dots, are taken from Tsuda & Ueda (2017).

#### 4.1.1. *Heat transfer mechanisms in thermoacoustic instability*

First, we compare the two mechanisms of heat transfer, namely conduction and phase exchange. In this comparison, shown in figure 2, we calculated $\Delta T_{onset}$ using the two methods presented in § 3.1 as a function of the Womersley number, here denoted by $\tau_v$. The results of conduction-driven thermoacoustics are obtained by setting $C_m \equiv 0$, reducing the equations to the known form of 'classical' thermoacoustics (Rott 1969). The experimental results, reported by Tsuda & Ueda (2017), show good agreement with the theoretical curves. In these experiments the working fluid comprises air and water vapour that evaporate/condense on the stack solid walls, matching the simple case of phase change derived by Raspet *et al.* (2002), which in our model corresponds to $\eta_n = 1$ (see § 2.1). This agreement validates our model's (as well as that of Raspet *et al.* 2002) ability to accurately capture the physical mechanisms in both conduction-driven and phase-exchange thermoacoustics.

Compared with the conduction-driven system, the phase exchange substantially decreases the onset temperature difference. This distinction is best understood comparing the conduction-driven and phase-exchange heat-to-acoustic work terms (see (2.59)). In the limit of ideal sorption, using (3.2) to express $\mathrm{d}C_m/\mathrm{d}x$ as a function of $\mathrm{d}T_m/\mathrm{d}x$ and assuming $Pr \approx Sc$, these terms differ only by the factor

$$\psi \approx \frac{C_m}{1 - C_m} \frac{l_h}{RT_m}, \tag{4.1}$$

| Fluid | $C_m$ ($T_m = 293$ K) | $l_h$ (kJ kg$^{-1}$) | $\psi$ ($T_m = 293$ K) | $T_b$ (K) | $l_h/(RT_b)$ | $l_h/(RT_b^2)$ (K$^{-1}$) |
|---|---|---|---|---|---|---|
| $H_2O$ | 0.0283 | 2255 | 0.486 | 373 | 13.11 | 0.0351 |
| EtOH | 0.0726 | 839 | 1.239 | 352 | 13.18 | 0.0374 |
| MeOH | 0.1491 | 1100 | 2.530 | 338 | 12.52 | 0.0370 |

TABLE 1. Characteristic values of parameters affecting the choice of reactive gas for phase-exchange thermoacoustic systems, shown for water, ethanol and methanol. Values are calculated for a mean pressure $p_m = 1$ bar.

which serves as a 'booster' for the temperature gradient, employing it to transfer heat through phase exchange of the reactive gas at the sorbent interface. The term $C_m/(1 - C_m)$ equals 1 for $C_m = 0.5$ and rapidly increases when the reactive gas constitutes more than half of the mixture. The non-dimensional group, $l_h/(RT_m)$, is typically much larger than 1 (see table 1). If $\psi = 1$ the two mechanisms contribute equally (approximately) to the conversion of heat to acoustic work, although choosing an appropriate reactive gas and setting the working conditions to increase $C_m$, one may easily achieve $\psi \gg 1$. As $\psi$ increases, more acoustic work is produced for the same temperature gradient or, in our case, onset is reached with a lower temperature difference along the stack.

Comparing between the two approaches taken for the stability analysis calculations, we notice the 'zero acoustic power' curves lie below their corresponding curves calculated using the numerical scheme. In the finite differences scheme $p_1(x)$ and $u_1(x)$ are the explicit solution to the boundary value problem in (3.3)–(3.4), while in the 'zero acoustic power' method these are assumed to obey a pure standing-wave behaviour, independent of $\tau_v$. This 'ideal wave' assumption leads to an artificial decrease in $\Delta T_{onset}$ since the method does not account for all the losses in the system. The better agreement with experimental results confirms the improved accuracy of the numerical scheme over the 'zero acoustic power' method.

Another point worth mentioning is that, while the conduction-driven curves are unbounded, with $\Delta T_{onset}$ tending to infinity for $\tau_v \to 0$ and $\tau_v \to \infty$, the temperature in phase-exchange systems is bounded by a 'depletion temperature', $T_{max}$, namely the temperature at which the sorbent can no longer sorb gas (or, equivalently, the boiling temperature, $T_b$, for a simple phase change process), such that $\Delta T_{onset} \leqslant T_{max} - T_c$. The Clausius–Clapeyron equation, used in our model, relates the partial pressure (in our scaled notation, $C_m$) to the temperature for an equilibrium state of saturation. If the fluid temperature surpasses $T_{max}$, the mean pressure must increase to allow the fluid to remain saturated. In our linear analysis the mean pressure is constant (see § 2.1); if we allow the gas mixture temperature to exceed $T_{max}$ the reactive gas will no longer be saturated and thus, it cannot condense into a liquid film. This limitation may, in principal, be corrected by extending the model to include $O(\varepsilon^2)$ terms, thus adding a second-order, $x$-dependent correction to the mean pressure.

4.1.2. *Effects of mixture composition*

We now examine different gas mixture compositions and how their properties affect the temperature difference required for onset. The inert gas in the mixtures is either air or helium, two commonly used gases in thermoacoustic systems (Arnott, Bass & Raspet 1992; Swift 1992). The reactive gases selected for this comparison are water, ethanol and methanol, all used as condensable vapours that undergo

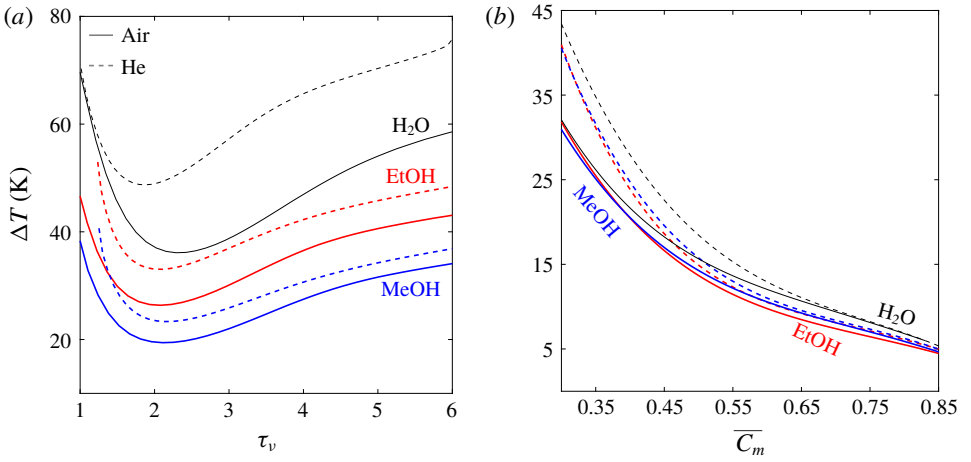


FIGURE 3. (Colour online) Stability curves for gas mixtures employing air (solid lines) and helium (dashed lines) as inert gases. The reactive gases are water (black), ethanol (red) and methanol (blue). The mean pressure is $p_m = 1$ bar, scaled stack length and location are $L_s/L = 0.04$ and $L_0/L = 0.8$, respectively, and ideal sorption is assumed ($\eta_v = \eta_D = 1$). Curves are plotted against: (*a*) the Womersley number, $\tau_v \equiv h(\omega/\nu)^{1/2}$, where the stack cold-side temperature is $T_c = 20\,^{\circ}\mathrm{C}$, and (*b*) the averaged concentration of the reactive gas in the stack, $\overline{C_m}$, for $\tau_v = 2.5$.

evaporation/condensation. Accordingly, $l_h$ is the latent heat of evaporation; for water this value is obtained from steam tables, while for ethanol and methanol it is calculated according to Majer & Svoboda (1985). All other gas mixture properties are calculated using the kinetic theory of gases (Poling, Prausnitz & O'Connell 2001). Characteristic values of the parameters affecting the choice of the reactive gases are listed in table 1.

Figure 3(*a*) presents stability curves of the selected gas mixtures as a function of $\tau_v$. Mixtures employing air as the inert gas outperform their matching helium-based mixtures in terms of $\Delta T_{onset}$. A possible explanation is helium's large heat capacity, compared with that of practically any gas, which requires a larger temperature difference for the same amount of heat to be transferred to the gas through conduction during an oscillation cycle, resulting in higher values of $\Delta T_{onset}$. The closer a mixture is to the reactive component's boiling temperature, the less dominant this effect is as the reactive gas becomes a larger fraction in the mixture, reflected through the concentration, $C_m$. As $C_m$ increases, more of the gas in the mixture participates in the isothermal phase-exchange heat transfer mechanism, as clearly indicated by the parameter $\psi \propto C_m/(1 - C_m)$ (see table 1 for characteristic values). In these calculations, the cold side temperature, $T_c$, is fixed at 20 °C for all mixtures, resulting in different values of $C_m$, determined by the proximity of $T_c$ to the fluid freezing and boiling temperatures. The value of $T_c$ was chosen for practical reasons as it is close to the ambient temperature, making it easier to maintain. While water at $p_m = 1$ bar coexists as liquid/vapour between $0 < T < 100\,^{\circ}\mathrm{C}$, EtOH and MeOH span a wider temperature range, and their boiling temperatures are significantly lower than that of $H_2O$ (see table 1). Accordingly, the values of $C_m$ in their mixtures for $T_c \leqslant T \leqslant T_b$ are substantially higher than for water (see table 1 for $C_m$ values at $T = T_c$), contributing to lower values of $\Delta T_{onset}$.

The results shown in figure 3(*b*) compare stability curves of the considered gas mixtures as a function of the averaged concentration of the reactive component in the stack, $\overline{C_m}$. The bar in $\overline{C_m}$ denotes axial averaging across the stack, and is an exception to its typical use for time averaging. All curves are calculated for $\tau_\nu = 2.5$, a value representative of good performance for all mixtures (see figure 3*a*). Here, different values of $\overline{C_m}$ are obtained by setting different temperatures as $T_c$, such that the temperatures on the stack are in the range $T_c \leqslant T \leqslant T_b$. As $T_c$ increases this range in narrowed, increasing $\overline{C_m}$, thus decreasing $\Delta T_{onset}$ as the phase-exchange mechanism is more dominant. At a certain point the temperature range narrows to match $\Delta T_{onset}$, setting the lowest possible temperature difference that would initiate onset, under the considered conditions. For all mixtures presented here the lowest temperature difference is $\Delta T_{min} \approx 5\,^{\circ}\mathrm{C}$, with $\overline{C_m} \approx 0.85$.

At low values of $\overline{C_m}$ the curves may be separated into two clearly visible groups: air- and helium-based mixtures. This separation is a consequence of the results shown in figure 3(*a*), where mixtures employing helium as the inert gas exhibited higher values of $\Delta T_{onset}$. As $\overline{C_m}$ increases, the reactive gas becomes a larger fraction in the mixture, gradually suppressing the differences between the two groups. At the highest concentration values for which onset is reached ($\overline{C_m} \approx 0.85$), all curves appear to converge to the same value. The values of $\Delta T_{onset}$ in this case are so low that the temperature gradient imposed on the stack is lower than the adiabatic temperature gradient experienced by the gas as it compresses and expands. Accordingly, the conduction-driven mechanism cannot convert heat to acoustic power, leaving only the phase-exchange mechanism to produce the required acoustic power that triggers the instability. This heat-to-acoustic power conversion is governed by the parameter $\psi$, dependent on $C_m$, $T_m$ and the reactive gas latent heat, $l_h$. Here $\overline{C_m}$ is practically equal for all mixtures, leaving the non-dimensional group $l_h/(RT_m)$ to distinguish between the gas mixtures and their performance. As $C_m$ on the stack is close to 1, all temperatures are very close to the reactive component's boiling temperature, $T_b$, such that $\psi$ may be approximated as

$$\psi \approx \frac{0.85}{1 - 0.85}\frac{l_h}{RT_b}, \tag{4.2}$$

where $\overline{C_m} \approx 0.85$ is the value for which $\Delta T_{min}$ is obtained. The non-dimensional group $l_h/(RT_b)$ displays similar values for all three reactive gases chosen (see table 1). As a result, all mixtures converge to a very similar value of $\Delta T_{min}$, although slight changes in $\Delta T_{min}$ between the different mixtures are perceptible. These changes may be explained by the factor $1/T_m$ multiplying $\psi$ in the phase-exchange heat-to-acoustic work term, which may also be approximated as $1/T_m \approx 1/T_b$. The small variations in the values of $l_h/(RT_b^2)$ for the three gases, listed in table 1, are reflected in the values of $\Delta T_{min}$ seen in figure 3(*b*).

#### 4.1.3. *Sorption kinetics*

The curves presented in figure 4 examine effects of reaction kinetics in a sorption process, where $\eta_\nu, \eta_D \neq 1$. These stability curves, calculated for different values of the partition coefficient $K$, are plotted against $R_k \equiv \nu/(h^2 k_d)$, a non-dimensional number linking the characteristic viscous and desorption time scales such that $\tau_k \equiv \sqrt{R_k}\tau_\nu$. All curves are calculated for an air–water mixture. $R_k \to 0$ and $R_k \to \infty$ denote the limits of fast and slow kinetics relative to the oscillation time scale, respectively. The dashed lines represent the two extreme cases for the sorbent/sorbate pair: 'ideal'

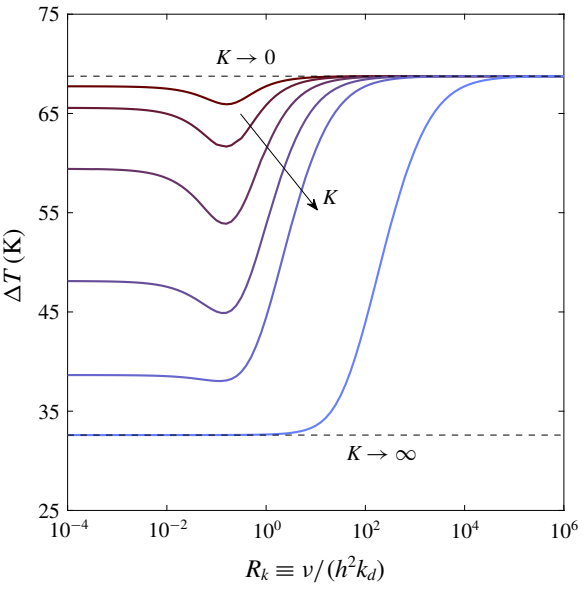


FIGURE 4. (Colour online) Stability curves for an air–water gas mixture at various values of the partition coefficient $K$, as a function of the kinetics non-dimensional number, $R_k$. The mean pressure is $p_m = 1$ bar, the Womersley number is $\tau_v = 2.5$, and scaled stack length and location are $L_s/L = 0.03$ and $L_0/L = 0.8$, respectively.

sorption ($K \to \infty$), in which the sorbent has no limitation on its capacity for sorbing gas (also applicable for evaporation/condensation from/to a liquid film, unbounded in its capacity for condensed vapour – see § 2.2), and no sorption ($K \to 0$), where the sorbent has zero capacity for sorbing the reactive gas such that (2.58) is reduced to the conduction-driven form (Rott 1969). All the curves approach the limit of $K \to 0$ for vanishingly slow kinetics (very large values of $R_k$), where the oscillations are too fast to allow mass exchange at the sorbent interface. In the case of fast kinetics, sorption occurs instantly, resulting in a quasi-steady state of equilibrium between the sorbent and gas phases. Accordingly, at low values of $R_k$ all curves flatten towards a specific value, determined by the partition coefficient, $K$, specifying the sorbent capacity for sorbing the reactive gas. If $K$ surpasses a certain value, here $K \approx 10^{-2}$, all curves are monotonically increasing, with the ascent towards the horizontal asymptote of $K \to 0$ occurring at different values of $R_k$. A curious limit is obtained for the case of ideal sorption occurring at an infinitesimally slow rate, for which the kinetics parameter does not recover $\eta_n \to 1$ nor $\eta_n \to \infty$, but rather an intermediate result, unaffected by the reaction rate and strongly dependent on the parameters $\Lambda$ and $N^s$, characterising the sorbent/sorbate pair.

While large values of $K$ result in monotonically increasing curves, small values of $K$ clearly show a minimum at $R_k \approx 10^{-1}$. Intuitively, one may assume the lowest temperature difference is always recovered for the limit of fast kinetics. For small $K$ values, however, the sorbent has very limited capacity for sorption, such that for $R_k \to 0$ mass exchange occurs in only a very small fraction of an oscillation cycle. During the remainder of the cycle, then, the sorbent is saturated and the phase-exchange mechanism is not active, resulting in an increase in $\Delta T_{onset}$ as $K$ decreases. An intentional, moderate increase in $R_k$, namely a regulated delay in

desorption rate, allows the sorbent to exchange mass with the gas mixture during a larger fraction of the oscillation cycle, thus lengthening the characteristic time in which the phase-exchange mechanism is active and consequently decreasing $\Delta T_{onset}$.

### 4.2. *Limit cycle analysis*

In this section we analyse the limit cycle of a phase-exchange system, i.e. the state at which the amplitude of oscillating quantities 'saturates' and becomes constant, typically obtained for $t \gg t_{onset}$, where $t_{onset}$ marks the stability limit breaching point in time. All results are calculated for an air–water mixture. Unless otherwise stated, the scaled stack length and location are $L_s/L = 0.04$ and $L_0/L = 0.83$, respectively, the limit of ideal sorption ($\eta_v = \eta_D = 1$) is assumed, and the heat flux input to the system is $Q_h = 25$ kW m$^{-2}$.

#### 4.2.1. *Acoustic field characteristics*

In the considered system configuration (shown in figure 1*a*) the no-penetration boundary conditions at the two closed ends impose a near-standing-wave behaviour of pressure and velocity. Viscous dissipation at the solid boundaries, the presence of a stack and its asymmetric location within the tube all contribute to a slight distortion of the wave form, deviating from a standing wave, and thus allowing the production (or dissipation) of non-zero acoustic power. However, this deviation is normally very small in standing-wave systems (such as the one considered here, see figure 1*a*), and the acoustic power flux

$$\dot{W} = \tfrac{1}{2}\mathrm{Re}[\widetilde{p_1}u_1] = \tfrac{1}{2}|p_1|\,|u_1|\cos(\phi) \tag{4.3}$$

is largely dependent on the phase angle between $p_1$ and $u_1$, $\phi$, which is typically in the range $|\phi| = 90° \pm 5°$ (Swift 1992).

Figures 5(*a*) and 5(*b*) present the axial distribution of pressure and velocity, respectively, in conduction-driven (red) and phase-exchange (blue) systems. Each curve is scaled by its respective maximum value, allowing a clear, visual comparison of the wave forms. For reference, we added curves of a pure standing wave (black, dotted), where $p_1$ and $u_1$ simply obey cosine and sine functions, respectively (see § 3.1.2). In both figures, the conduction-driven curves only slightly deviate from the standing-wave curves; the largest deviation is unsurprisingly spotted in the stack, where acoustic oscillations are enhanced. The phase-exchange curves, calculated for a large value of the 'reactive' gas concentration ($\overline{C_m} = 0.91$) to demonstrate the magnitude of the effect, deviate strongly from the standing-wave curves. While in conduction-driven systems the stack may be thought of as an acoustic power point source, amplifying random displacements of gas parcels, in phase-exchange systems it also acts as a mass point source. The periodic mass exchange with the sorbent layer draws/releases mass from/to the gas mixture, consequently increasing the reactive gas mass flux in the stack, which translates directly to a sharp increase in velocity (both real and imaginary), seen clearly in figure 5(*b*) at $\widehat{x} \approx 0.83$. The asymmetric location of the stack within the system shifts the imaginary component, quasi-sinusoidal velocity distribution towards the stack, where the velocity increases. As a result, the pressure distribution is also shifted from its quasi-cosine profile, and the absolute value of the pressure at the two closed ends clearly shows $|p_1(\widehat{x} = 0)| > |p_1(\widehat{x} = 1)|$, corresponding to the increase in velocity near $\widehat{x} = 1$.

Figure 5(*c*) shows the phase angle between $p_1$ and $u_1$ along the system, for several values of $\overline{C_m}$, the mean concentration of the reactive gas in the stack. As in figures

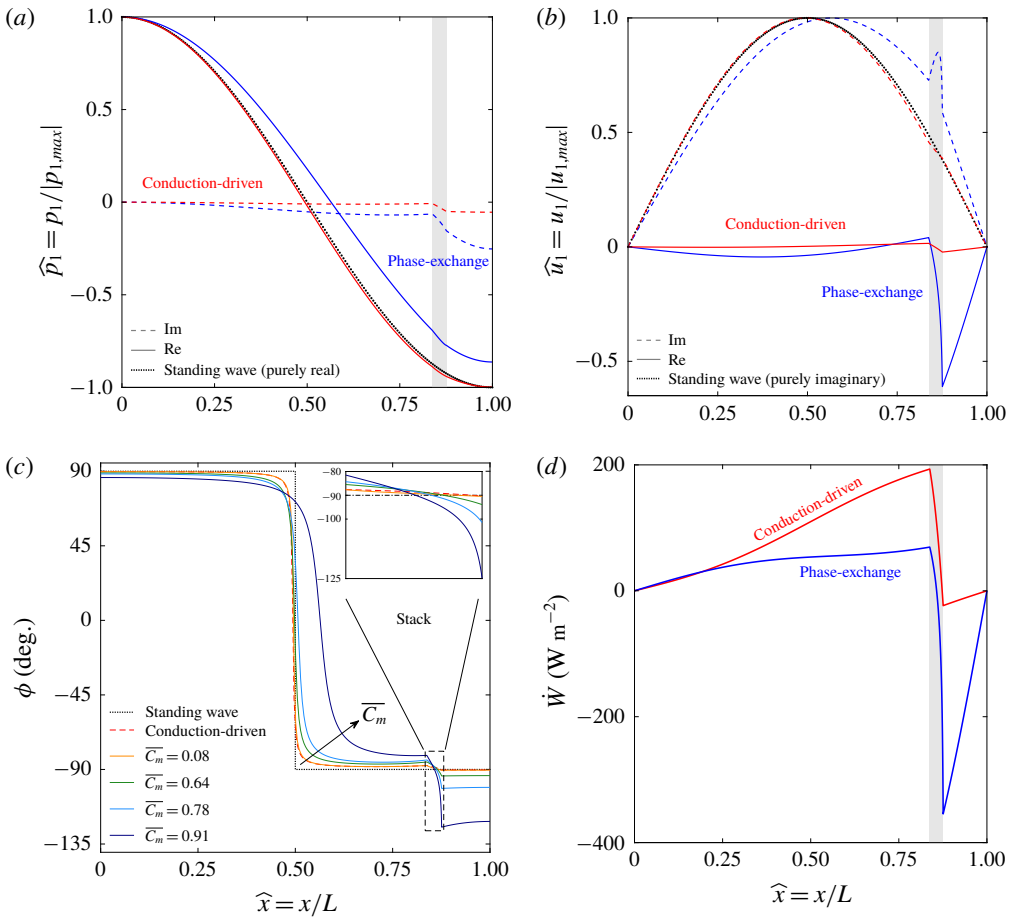


FIGURE 5. (Colour online) Acoustic field characteristics for conduction-driven (red) and phase-exchange (blue) systems, compared to a pure standing wave (black, dotted): (*a*) real (solid line) and imaginary (dashed line) components of the pressure amplitude, scaled by the maximum pressure in the system, (*b*) real (solid line) and imaginary (dashed line) components of the velocity amplitude, scaled by the maximum velocity in the system, (*c*) phase angle between pressure and velocity, $\phi$, throughout the system, and in the stack in particular (inset), for different mean concentrations of the reactive gas, $\overline{C_m}$, and (*d*) acoustic power. The highest $\overline{C_m}$ value presented in (*c*) corresponds to the phase-exchange curves in (*a*,*b*,*d*). All properties are drawn against $\widehat{x} = x/L$, the axial coordinate scaled by the system length. The shaded area marks the stack location in the system. The mean pressure is $p_m = 1$ bar, $\tau_v = 2$, the scaled stack length and location are $L_s/L = 0.04$ and $L_0/L = 0.83$, respectively, the heat flux input is $Q_h = 25$ kW m$^{-2}$, and ideal sorption is assumed ($\eta_v = \eta_D = 1$).

5(*a*) and 5(*b*), a pure standing-wave curve (black, dotted) and conduction-driven (red, dashed) curves are drawn for comparison. The inset displays a close-up view of the stack, where the phase angle changes rapidly. As reflected from the results of figure 5(*a*,*b*), the conduction-driven curve only slightly deviates from the standing-wave curve. In fact, the largest deviation, neglecting the sharp decrease near $\widehat{x} = 0.5$ (where the pressure moves from leading the velocity to trailing it), is only

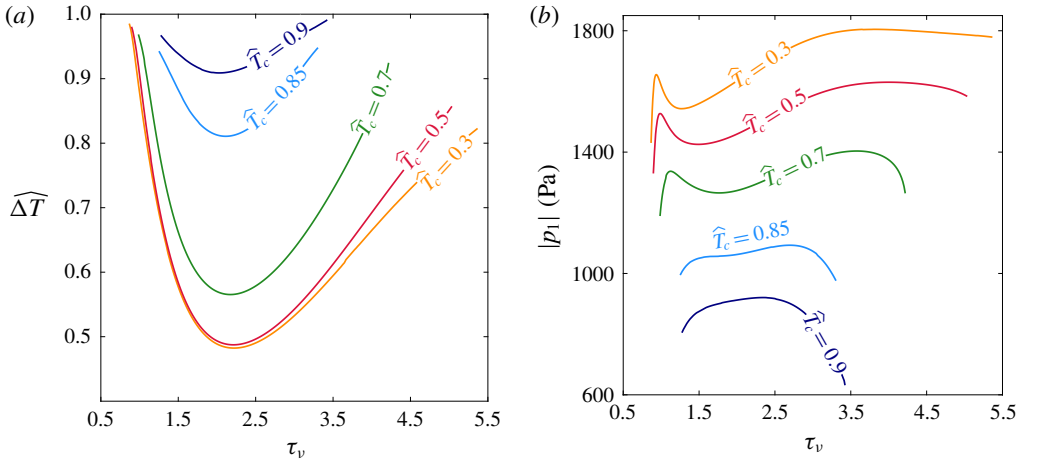


FIGURE 6. (Colour online) Limit cycle scaled temperature difference across the stack (*a*) and maximum pressure amplitude (*b*) as a function of the Womersley number, $\tau_v$, for different scaled cold side temperatures, $\widehat{T}_c = (T_c - T_{min})/(T_{max} - T_{min})$. The mean pressure is $p_m = 1$ bar, the scaled stack length and location are $L_s/L = 0.04$ and $L_0/L = 0.83$, respectively, the heat flux input is $Q_h = 25$ kW m$^{-2}$ and ideal sorption is assumed ($\eta_v = \eta_D = 1$).

2.4°. At the lowest concentration considered ($\overline{C_m} = 0.08$), the phase-exchange case is nearly identical to the conduction-driven curve. At such a low concentration, altering the working gas contributes merely to a decrease in the temperature difference along the stack (discussed in § 4.2.2), while the wave form is left unaffected. As $\overline{C_m}$ is increased, the phase angle distribution departs from the standing-wave behaviour, until at $\overline{C_m} = 0.91$ a remarkable 35° deviation from a pure standing wave ($\phi = -125°$) is obtained at the stack hot end. This difference in phase angles between the conduction-driven and phase-exchange mechanisms translates into an increase in acoustic power, as shown in figure 5(*d*) (calculated using (4.3)). Although the absolute pressure amplitudes decrease as $\overline{C_m}$ increases (not visible in figure 5*a* due to scaling; discussed in § 4.2.2), the dramatic increase in phase angle leads to a higher acoustic power produced by the phase-exchange system.

### 4.2.2. *Temperature difference and pressure amplitude*

Here, we calculate the temperature difference across the stack and the maximum pressure amplitude ($\Delta T$ and $|p_1|$, respectively), so as to establish a more complete description of the system limit cycle. Figure 6(*a*,*b*) presents these two quantities as a function of the Womersley number, $\tau_v$. For each calculation, the boundary condition for the stack cold side temperature, $T_c$, is varied. For the sake of even comparison, both the cold-side temperature and the temperature difference on the stack are scaled as follows

$$\widehat{T}_c = \frac{T_c - T_{min}}{T_{max} - T_{min}}, \quad \widehat{\Delta T} = \frac{\Delta T}{T_{max} - T_c}, \tag{4.4a,b}$$

where $T_{max}$ is the reactive fluid 'depletion temperature' (see § 4.1.1), and $T_{min}$ is its triple-point temperature, below which the reactive gas component is completely in the sorbed phase and $C_m = 0$. For the case of simple phase change through

evaporation/condensation $T_{min}$ is simply the freezing temperature. The shape of the curves in figure 6(*a*) resembles that of the stability curves in figures 2 and 3(*a*): each curve has a unique $\tau_v$ value, for which the limit cycle temperature difference is minimised. Here $\tau_v \approx 2$ marks the minimum in all curves, a representative result for a standing-wave system (Swift 2002). When $\tau_D \equiv \tau_v Sc^{1/2}$, the ratio of the characteristic time scales for molecular diffusion and acoustic oscillations is either too small or too large, $\Delta T$ increases, so as to compensate for the poor match between these time scales.

The asymmetric increase in $\widehat{\Delta T}$ for $\tau_v < 2$ and $\tau_v > 2$ is a result of the match between $\tau_D$ and the system travelling-wave component, manifested by the deviation of the wave form from that of a pure standing wave,

$$\theta = ||\phi| - 90°|. \tag{4.5}$$

In a pure travelling-wave system, perfect thermal contact of the working gas with the boundary is required, i.e. $\tau_v$, $\tau_\alpha$, $\tau_D \ll 1$ (Swift 2002). For a given $\widehat{T}_c$, as $\widehat{\Delta T}$ increases so does $\overline{C_m}$, subsequently increasing $\theta$. For $\tau_v < 2$, the increased $\theta$ favours the decrease in $\tau_v$ and the system sustains a limit cycle until $\widehat{\Delta T}$ nearly approaches 1, marking its highest possible temperature difference. For $\tau_v > 2$ each curve reaches a different $\widehat{\Delta T}$ before a limit cycle is no longer sustained at the given heat input. Each $\widehat{T}_c$ value corresponds to a characteristic $\overline{C_m}$ value, to which a specific $\theta$ matches. At $\widehat{T}_c = 0.3$–$0.7$, $\theta$ is relatively small and, while the curves depart from their optimal standing-wave point ($\tau_v \approx 2$), the moderate increase in $\theta$ does not favour the increase in $\tau_v$, and a limit cycle cannot be sustained before $\widehat{\Delta T}$ approaches 1. At $\widehat{T}_c > 0.85$, $\theta$ is initially large and the curves do not deviate substantially from $\tau_v = 2$. As $\widehat{\Delta T}$ increases, the increase in $\theta$ dramatically decreases the resonant frequency (discussed in § 4.2.3), thus reducing the system losses – proportional to $\omega$ – and enabling the curves to approach $\widehat{\Delta T} = 1$ (the $\widehat{T}_c = 0.9$ in particular).

The maximum pressure amplitude in the system is shown in figure 6(*b*) as a function of $\tau_v$, for different values of $\widehat{T}_c$. As the mean pressure is kept constant, $T_{max}$ is also a constant and as $\widehat{T}_c$ is increased, the system thermal potential decreases. As a result, the system can produce lower pressure amplitudes such that $|p_1|$ systematically decreases as $\widehat{T}_c$ is increased. For $\widehat{T}_c = 0.3$–$0.7$, the curves exhibit a local minimum that vanishes as $\widehat{T}_c$ is further increased. The $\overline{C_m}$ values near the minima in these curves are small and the system resembles a conduction-driven system, in which the curve for $|p_1|$ tends to infinity for $\tau_v \to 0, \infty$ and displays a minimum at $\tau_v \approx 2$. However, this resemblance disappears as $\tau_v$ is shifted from the minimum and the curves point downwards near their critical $\tau_v$, where $\widehat{\Delta T}$ reaches its highest values. The increase in $\widehat{\Delta T}$ increases $\theta$, and as the wave form deviates from a standing wave, the produced pressure amplitudes decrease. The two maximum points linking a curve's ends with its minimum are noticeably different. At the left point ($\tau_v \approx 1$), the increase in $\theta$ matches the decrease in $\tau_v$ towards values favouring travelling-wave phasing, locally increasing $|p_1|$. The right point marks the global maximum in each curve, and is the result of an increase in thermal potential, while $\theta$ only moderately increases, retaining the resemblance to a standing-wave system and thus increasing $|p_1|$. As $\theta$ is further increased, $|p_1|$ again decreases until a limit cycle can no longer be sustained. For $\widehat{T}_c = 0.85$–$0.9$, any resemblance to a conduction-driven system disappears: the local minimum vanishes, leaving only a maximum point from which the curves decrease in either direction.

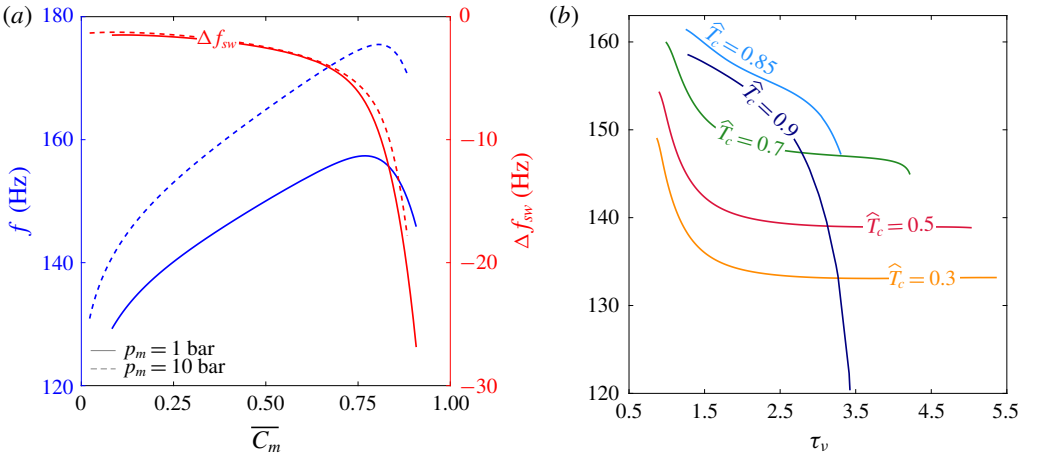


FIGURE 7. (Colour online) (*a*) Resonant frequency (blue, left axis) and the deviation from the frequency of an 'ideal' standing wave (red, right axis) as a function of the averaged reactive gas concentration in the stack, $\overline{C_m}$, for $\tau_v = 2$ at mean pressures 1 and 10 bar. (*b*) Resonant frequency at $p_m = 1$ bar as a function of the Womersley number, $\tau_v$, for different scaled stack cold side temperatures, $\widehat{T}_c = (T_c - T_{min})/(T_{max} - T_{min})$. Curves are calculated for scaled stack length and location $L_s/L = 0.04$ and $L_0/L = 0.83$, respectively, heat flux input $Q_h = 25$ kW m$^{-2}$ and for ideal sorption ($\eta_v = \eta_D = 1$).

4.2.3. *Frequency response*

In general, the resonant frequency of a thermoacoustic system is determined by its geometry and the sound velocity through its working fluid. Most thermoacoustic systems employ a gaseous working fluid, in which the sound velocity is $a = \sqrt{\gamma R_g T_m / M_{mix}}$, such that the resonant frequency approximately scales as $\omega \propto M_{mix}^{-1/2}$. The resonant frequency of a phase-exchange system is calculated and plotted in figure 7(*a*) (blue) as a function of $\overline{C_m}$, for two representative mean pressures. At $\overline{C_m} \lesssim 0.65$, the two curves seem to follow the rationale described above: water vapour is lighter than air and thus increasing its fraction in the gas mixture increases the resonant frequency. However, at $\overline{C_m} \approx 0.8$ a maximum appears, after which an increase in water concentration leads to a decrease in frequency until eventually, at very large $\overline{C_m}$ values, the system can no longer sustain a limit cycle, at the given heat input.

The resonant frequency at the limit cycle inherently deviates from that of a pure standing wave since the latter cannot be practically sustained. This deviation, $\Delta f_{sw} = f - f_{sw}$, is drawn in the right axis of figure 7(*a*) (red), and assists in understanding the competing phenomena leading to this unusual frequency response. In a diluted gas mixture ($\overline{C_m} \ll 1$), the wave form resembles a standing wave, reflected through small values of $\Delta f_{sw}$. Since a pure travelling-wave behaviour would substantially decrease the frequency, the minor travelling-wave component here slightly decreases it. As $\overline{C_m}$ increases, the travelling-wave component increases and the frequency deviates more and more from that characterising a standing wave. Towards higher vapour concentrations, $\Delta f_{sw}$ decreases sharply until, near $\overline{C_m} \approx 0.8$, the increase in water vapour in the mixture, which tends to increase the resonant frequency, is balanced by a decrease emerging from the wave-form distortion. At the highest attainable concentrations, the wave is greatly distorted (see figure 5), leading

to a considerable decrease in frequency despite the water-enriched mixture tending to increase it.

The same trend is obtained at higher mean pressures. As a representative example, curves calculated at a mean pressure $p_m = 10$ bar (dashed) are drawn, displaying a similar behaviour but at slightly higher frequencies. Increasing the mean pressure inherently increases the depletion (or boiling) temperature $T_{max}$; for a given $\overline{C_m}$, such increase in $p_m$ directly translates to an increase in $T_m$ (see (3.1)), subsequently increasing the sound velocity and thus increasing the resonant frequency. The largest $\overline{C_m}$ for which a limit cycle is attained moderately decreases with increasing $p_m$. These terminal $\overline{C_m}$ values correspond to $\Delta T_{min} \approx 4.5$, 25 °C for $p_m = 1$, 10 bar, respectively. A good indicator for estimating these temperature differences is the parameter $\psi = (C_m/(1 - C_m))(l_h/RT_m)$, representing the ratio of produced acoustic power by the conduction-driven and phase-exchange heat transfer mechanisms (see § 4.1.1). Since $\psi$ is a monotonically decreasing function of $p_m$ (see appendix A), a larger $\Delta T$ is required as $p_m$ increases, translating to a lower $\overline{C_m}$.

Studying the resonant frequency response to core variables affecting the system performance, we calculate $f$ as a function of the Womersley number, $\tau_v$, for different scaled cold-side temperatures, $\widehat{T}_c$, and present the curves in figure 7(*b*). Increasing $\widehat{T}_c$ imposes a larger initial value of $\overline{C_m}$ on a system. As reflected in the results of figure 7(*a*), increasing $\widehat{T}_c$ in figure 7(*b*) initially increases $f$ until, for $\widehat{T}_c = 0.9$ (corresponding to $\overline{C_m} \sim 0.9$), the resonant frequency decreases. The $\widehat{T}_c = 0.3$ and $\widehat{T}_c = 0.5$ curves display a similar trend of initial decrease and eventual flattening. The largest $\overline{C_m}$ in these curves is obtained at $\tau_v \approx 0.9$ (where $\widehat{\Delta T}$ approaches 1 in figure 6*a*); as $\tau_v$ increases, $\Delta T$ decreases towards its minimum at $\tau_v \approx 2$, consequently decreasing $\overline{C_m}$. As a result, the resonant frequency decreases as the water vapour fraction in the mixture is reduced. Further increasing $\tau_v$ shifts the system from its optimal standing-wave working point, and $\Delta T$ increases accordingly. This increases $\overline{C_m}$, acting to further increase the frequency by increasing the mixture water vapour fraction while tending to decrease it by increasing the deviation from a standing wave. These two factors are balanced and the frequency remains approximately constant until a limit cycle can no longer be sustained at the given heat input. For $\widehat{T}_c > 0.5$ the $\tau_v$ range for which a limit cycle may be sustained narrows, and $\widehat{\Delta T}$ is confined within a smaller range. Consequently, the curves' initial slope diminishes as the decrease in $\overline{C_m}$ subsides. For $\tau_v > 2$, the increase in the travelling-wave components is augmented as $\widehat{T}_c$ increases, and tends to decrease $f$. While for $\widehat{T}_c = 0.7$ the increase in $\overline{C_m}$ is significant, resulting in a moderate decrease in $f$ (resembling the $\widehat{T}_c < 0.7$ curves), the travelling-wave component growth at $\widehat{T}_c > 0.7$ dominates the frequency response, leading to a sharp decrease in $f$ as $\tau_v$ increases.

#### 4.2.4. *Varying heat flux input*

Part of the heat input to a thermoacoustic system is converted into acoustic power, sustaining the oscillations, and the rest is ejected as waste heat. For a given system with constant mean pressure, increasing the heat input to the system may increase the stack hot-side temperature, and/or the pressure and velocity amplitudes. The curves in figure 8(*a*) display $\widehat{\Delta T}$ as a function of the heat flux input to the system, $Q_h$, for different $\overline{C_m}$ values. In all curves $Q_h = 0$ trivially results in $\widehat{\Delta T} = 0$; as $Q_h$ is increased $\widehat{\Delta T}$ initially increases (dashed), until the heat flux input reaches a critical value, $Q_{crit}$, from which a limit cycle can be sustained. When $Q_{crit}$ is surpassed, $\widehat{\Delta T}$ moderately

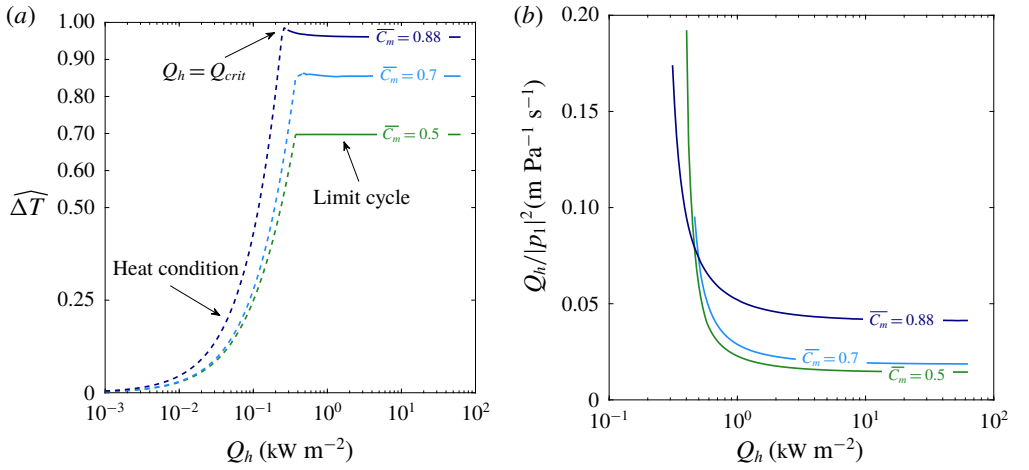


FIGURE 8. (Colour online) (*a*) Scaled temperature difference across the stack, defined in (4.4), and (*b*) the heat flux input, scaled against the maximum pressure amplitude squared, as a function of the heat flux input, $Q_h$, for different reactive gas concentrations. While in (*b*) only the limit cycle results (solid lines) are displayed, the dashed lines in (*a*) represent solutions to a one-dimensional conduction equation, obtained for $Q_h < Q_{crit}$. The mean pressure is $p_m = 1$ bar, $\tau_v = 1.4$, the scaled stack length and location are $L_s/L = 0.04$ and $L_0/L = 0.83$, respectively, and ideal sorption is assumed ($\eta_v = \eta_D = 1$).

decreases before flattening towards a constant, representative value for each $\overline{C_m}$. The weak dependency of $\widehat{\Delta T}$ on $Q_h$ is somewhat unintuitive, and may be explained by considering (2.65), namely the total power flux equation. The equation may easily be manipulated into the form

$$\frac{\mathrm{d}T_m}{\mathrm{d}x} = \frac{Q_h - f_1(p_1, u_1, T_m)}{f_2(u_1, T_m) + \text{diffusion terms}}, \tag{4.6}$$

where $f_1$ and $f_2$ are complex functions of the pressure, velocity and temperature (given explicitly in (2.65)), and the diffusion terms are a function of the temperature alone. Using (3.3) we may consider $f_1(p_1, \mathrm{d}p_1/\mathrm{d}x, T_m)$ and $f_2(\mathrm{d}p_1/\mathrm{d}x, T_m)$, explicitly dependent on $p_1$ and its derivative, and only implicitly dependent on $T_m$ through the gas mixture properties. Since this implicit relation is relatively weak, we assume $f_1, f_2 \neq f(T_m)$ and turn to focus on the pressure dependency.

The pressure distributions in figure 5(*a*) display the two extremes of a phase-exchange system: conduction-driven system, where the phase-exchange mechanism is absent, and nearly isothermal system, in which only the phase-exchange mechanism converts heat to acoustic power. As opposed to velocity (figure 5*b*), the pressure distribution is only weakly affected by the change in heat transfer mechanism. Its wave form can therefore be described, to a good degree of accuracy, by considering a pure standing wave, as given in (3.9). For $Q_h < Q_{crit}$, a limit cycle cannot be sustained and (4.6) reduces to a one-dimensional heat equation in a binary gas mixture, in which $p_1 = 0$. Increasing $Q_h$ in this region trivially increases $\widehat{\Delta T}$. At $Q_h = Q_{crit}$ a jump in $p_1$ (followed by an increase as $Q_h$ increases) is obtained, leading to a local decrease in $\widehat{\Delta T}$, indicated clearly in (4.6). As $Q_h$ is further increased,

$p_1$ increases, swiftly overweighing the effect of the diffusion terms on $\widehat{\Delta T}$, and the temperature gradient simplifies to

$$\frac{\mathrm{d}T_m}{\mathrm{d}x} \approx G_1 \frac{Q_h}{p_A^2} - G_2, \quad Q_h \gg Q_{crit}, \tag{4.7}$$

where $p_A$ is the standing-wave pressure amplitude, and $G_1$ and $G_2$ contain the spatial distribution of $p_1$ and its derivative, as well as the losses multiplying $p_A^2$, assumed independent of $T_m$. If $Q_h \propto p_A^2$, $\mathrm{d}T_m/\mathrm{d}x \approx$ const. and $\widehat{\Delta T}$ is nearly a constant. To illustrate this relation, we calculated $Q_h/|p_1|^2$, namely the heat flux input divided by the limit cycle square maximum pressure amplitude, and plotted it against $Q_h$ in figure 8(*b*). Theoretically, such curves tend to infinity at $Q_h = Q_{crit}$; for practical reasons, only results above a threshold of $|p_1| = 100$ Pa are displayed. The curves quickly decay towards a constant value, in agreement with (4.7). This flat shape of the curves remains as $Q_h$ is further increased, and the approximation is valid as long as $p_1/p_m = O(\varepsilon)$. It is worthwhile noting, that the same behaviour is observed for a conduction-driven system; the general form of (4.6) results in a nearly identical approximation, in which only the values of $G_1$ and $G_2$ in (4.7) vary.

4.2.5. *Sorption kinetics*

In order to study the effects of reaction kinetics on the system's limit cycle, we relax the assumption of ideal sorption ($\eta_v$, $\eta_D \neq 1$) and calculate key elements that characterise the limit cycle – $\Delta T$ and $|p_1|$, as affected by the sorption characteristics. Figure 9(*a*) presents the scaled temperature difference across the stack, $\widehat{\Delta T}$, as a function of $R_k/K \equiv \nu/(h^2 k_a)$, the ratio of the viscous time scale and the (forward) sorption reaction, for various values of $K$. Although drawn against $R_k/K$ (instead of simply against $R_k$), the curves resemble their respective curves from the stability analysis (figure 4): the left end of the curves represents the limit of fast kinetics, in which each curve flattens towards a unique $\widehat{\Delta T}$ value, determined by the value of $K$ – the boundary's sorptive affinity for a given gas component. The right end of the curves represents the limit of slow kinetics, a limit to which all curves approach. However, unlike figure 4, at the system limit cycle $K \to 0$ does not recover the known, conduction-driven thermoacoustics solution (dashed-dotted, red). The oscillatory flow, produced solely by the conduction-driven mechanism in this limit, in the presence of a temperature gradient, results in a hydrodynamic dispersion of heat down the gradient. Since $\mathrm{d}C_m/\mathrm{d}x \propto \mathrm{d}T_m/\mathrm{d}x$, a concentration gradient is also imposed on the stack, giving rise to molecular diffusion as well as dispersion of mass down the concentration gradient. This undesired mass transfer requires more heating power to evaporate/desorb more of the reactive component, such that $\mathrm{d}T_m/\mathrm{d}x$ decreases, and eventually $\Delta T_{(K\to 0)} < \Delta T_{(conduction\text{-}driven)}$.

As in all phase-exchange results, $\widehat{\Delta T} \leqslant 1$ is bounded by the reactive fluid depletion temperature, $T_{max}$ (see § 4.1.1). Additionally, the stability analysis showed that all curves are further bounded by the limit $K \to 0$, recovering the conduction-driven result. Here $K \to 0$ does not recover the conduction-driven result, and, surprisingly, the curves are not physically bounded by the $K \to 0$ nor by the conduction-driven lines. Curves of small, finite $K$ values occasionally exceed these lines for sufficiently fast kinetics ($R_k/K \lesssim 10$). In order to closely examine this phenomenon, we consider the limit of fast kinetics ($R_k \to 0$), neutralising the effect of reaction kinetics and focus attention to the effect of $K$ and $\tau_v$ on $\widehat{\Delta T}$. We calculate $\widehat{\Delta T}$ as a function of

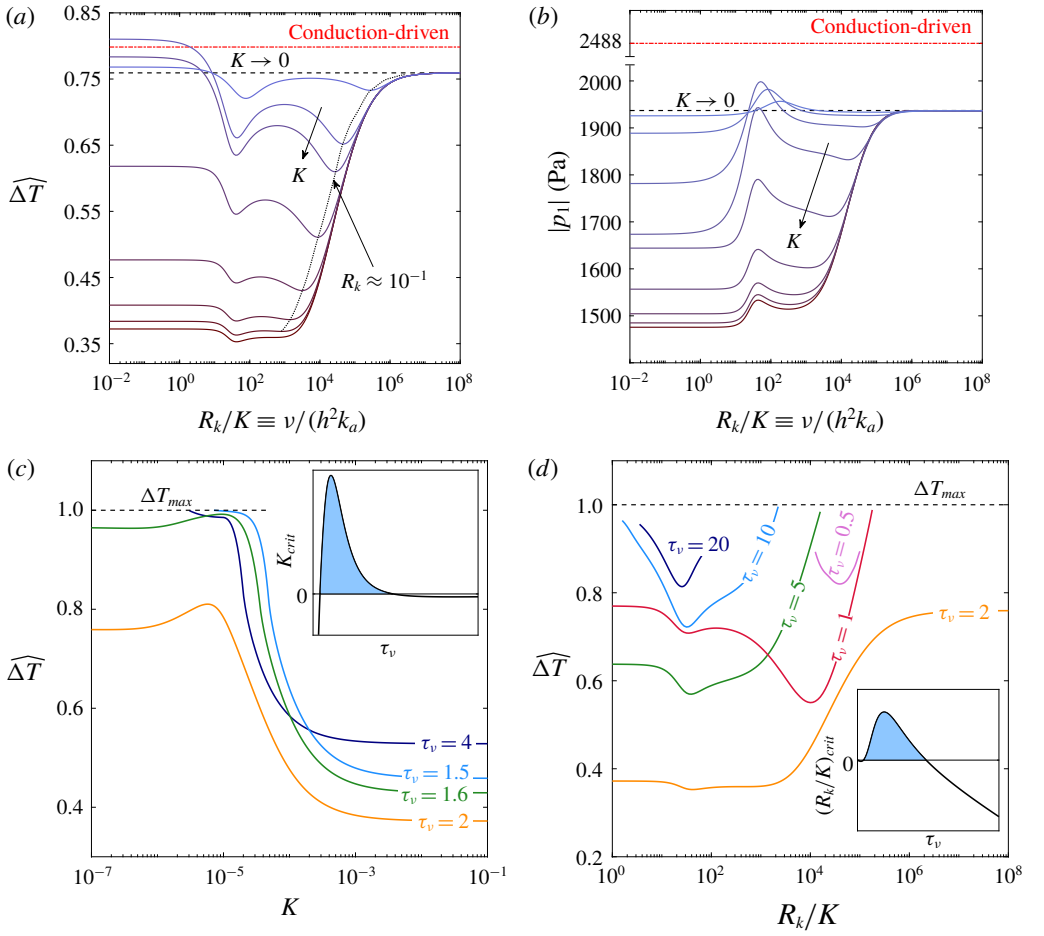


FIGURE 9. (Colour online) (*a*) Scaled temperature difference across the stack, $\widehat{\Delta T} = \Delta T/(T_{max} - T_c)$, and (*b*) maximum pressure amplitude, $|p_1|$, as a function of the non-dimensional group $R_k/K$ for different values of the partition coefficient $K$, at $\tau_\nu = 2$. (*c*) Value of $\widehat{\Delta T}$ for the limit of fast kinetics ($R_k \to 0$) as a function of $K$ for different $\tau_\nu$ values. The inset presents an analytic approximation for the critical partition coefficient, $K_{crit}$, for which a maximum appears, as a function of $\tau_\nu$. (*d*) Value of $\widehat{\Delta T}$ for the limit of ideal sorption ($K \to \infty$) as a function of $R_k/K$ for different $\tau_\nu$ values. The inset presents an analytic approximation for the critical value $(R_k/K)_{crit}$ for which a minimum appears, as a function of $\tau_\nu$. The mean pressure is $p_m = 1$ bar, the cold-side temperature is $T_c = 20\,^\circ$C, the scaled stack length and location are $L_s/L = 0.02$ and $L_0/L = 0.83$, respectively, and the heat flux input is $Q_h = 25$ kW m$^{-2}$.

$K$, and plot different curves in figure 9(*c*), each representing a unique $\tau_\nu$ value. The $\tau_\nu = 2$ curve matches the $R_k/K \to 0$ limit results in figure 9(*a*). All the curves in figure 9(*c*) approach a constant value as $K \to \infty$ (i.e. ideal sorption), determined by the value of $\tau_\nu$. Interestingly, some curves display a maximum point while others are cut off as the curve approach $\widehat{\Delta T} = 1$. Theoretically, all curves exhibit a maximum point, although for certain $\tau_\nu$ this point may be obtained at $\widehat{\Delta T} > 1$ or $K < 0$, both representing non-physical cases. These $\tau_\nu$, either too small or too large, yield a relatively large $\widehat{\Delta T}$ even when $K \to \infty$ (see figure 6*a*, where $\eta_\nu = \eta_D = 1$ is assumed),

and as the boundary's affinity for sorption is decreased, the short distance to the $\widehat{\Delta T} = 1$ line is insufficient for a maximum to appear. This result is confirmed by an analytic approximation detailed in appendix B. The results of this approximation, presented in the inset of figure 9(*c*), show the qualitative trend of $K_{crit}$, the $K$ value leading to a maximum in the curves of figure 9(*c*), as a function of $\tau_v$ for $Sc = 0.6$. As clearly seen, a positive (physical) value of $K_{crit}$ (shaded) is obtained only for a finite, intermediate range of $\tau_v$. This result is reproduced for any $Sc > 0$.

The curves in figure 9(*a*) generally display two minima: the first appears at $R_k/K \approx 50$ in all curves, and the second appears at $R_k \approx 10^{-1}$, marked by a dotted line connecting the points. While the two minima are suppressed in the limit of $K \to 0$, only the second minimum is flattened for $K \to \infty$. For $K \to 0$, $\eta_n \to \infty$ and $\eta_v/\eta_D \to (1 - F_v)/(1 - F_D)$ are recovered, regardless of the value of $R_k$. This limit truly suppresses the effect of reaction kinetics since the material now has no sorption affinity, and the minima vanish. If $K$ is small but finite, the value of $R_k$ dramatically affects $\widehat{\Delta T}$; the second minimum ($R_k \approx 10^{-1}$) appears also in the stability analysis calculations (figure 4), and is a result of the boundary's limited sorption capacity, that may be compensated by a regulated delay in desorption rate (see detailed explanation in § 4.1.3). When $K > 10^{-1}$, this minima disappears, leaving a short flat region before increasing towards the limit of $K \to 0$. The first minimum ($R_k/K \approx 50$), absent in the stability analysis calculations, remains for all $K$. Investigating the nature of this minimum, we calculate additional curves of $\widehat{\Delta T}$ versus $R_k/K$ for the limit of ideal sorption ($K \to \infty$) at various $\tau_v$ values. All these curves, presented in figure 9(*d*), show at least one minimum. For $\tau_v > 2$, the minimum shifts towards small $R_k/K$. Here the boundary has a high affinity for sorption, and the value of $\tau_v$ sets the oscillation rate, for which an optimum of the reaction kinetics exists, such that $\widehat{\Delta T}$ is minimised. As $\tau_v$ is increased, the optimum is obtained for faster kinetics, or smaller $R_k/K$ values. Theoretically, there exists a critical value $(\tau_v)_{crit}$, for which $R_k/K = 0$; if $\tau_v > (\tau_v)_{crit}$, the minimum point lies at $R_k/K < 0$ – a non-physical result. Practically, since $\widehat{\Delta T} \leqslant 1$ sets a physical constraint, $\tau_v > (\tau_v)_{crit}$ curves do not yield any valid limit cycle results, and therefore curves showing no minimum cannot be drawn. For $\tau_v < 2$, the second minimum point, suppressed for $K \to \infty$ at $\tau_v \geqslant 2$, reappears and as $\tau_v$ is further decreased the first minimum vanishes, leaving a single minimum that shifts towards large $R_k/K$. If $\tau_v$ is dramatically decreased, the minimum is pushed towards very large values of $R_k/K$, in which the curves approach the $K \to 0$ limit, where the minimum is, again, suppressed. As before, the $\widehat{\Delta T} \leqslant 1$ constraint makes it impossible to draw such curves, as their results exceed $\widehat{\Delta T} = 1$ well before the minimum disappears. In the absence of numerical evidence to support our claim, we seek an analytic approximation proving that a minimum is obtained for only a finite range of $\tau_v$. The details of this approximation appear in appendix B, and its results, presented in the inset of figure 9(*d*), show $(R_k/K)_{crit}$, namely the $R_k/K$ value leading to a minimum in the curves of figure 9(*d*), as a function of $\tau_v$ for $Sc = 0.6$. These results indicate that a minimum in $\widehat{\Delta T}$ should only be obtained for a finite, intermediate range of $\tau_v$, since $(R_k/K)_{crit} < 0$ does not represent a physically valid solution.

The effect of reaction kinetics on a thermoacoustic system vary according to the system's objective: for minimising $\Delta T$, controlling $R_k$ proves to be beneficial even if $K \to \infty$, but works to the contrary if one wishes to maximise $\dot{W}$, since the minimum in $\widehat{\Delta T}$ imposes an undesired minimum on $\theta \equiv ||\phi| - 90°|$ such that $\dot{W}$ is also lowered. This effect is clearly seen in figure 9(*b*), showing the maximum pressure amplitude,

$|p_1|$, as a function of $R_k/K$. The nearly monotonically increasing nature of the curves, linking the limits of fast and slow kinetics, is disturbed by a local maximum point, exactly matching the minimum points at $R_k/K \approx 50$ in figure 9(*a*). The increase in $|p_1|$ cannot be attributed to the decrease in $\widehat{\Delta T}$ directly, since the latter decreases the system's thermal potential. However, the subsequent effect of the minimum in $\widehat{\Delta T}$ on $\phi$ alters the wave form such that a nearly pure standing wave is obtained, for which $|p_1|$ increases in spite of the decrease in $\dot{W}$. All values of $|p_1|$ here are smaller than the conduction-driven reference values. Although $\widehat{\Delta T}$ may exceed the conduction-driven value for $R_k \to 0$, thus maximising the system thermal potential, the wave form deviates from a standing wave appreciably, resulting in a small, minimal value of $|p_1|$. At the local maximum ($R_k/K \approx 50$), the resemblance of wave form to a pure standing wave increases $|p_1|$, such that for finite $K$ values the $K \to 0$ limit is breached. The local minimum in $\widehat{\Delta T}$ decreases the system thermal potential, such that the maximal phase-exchange pressure amplitude ($|p_1| \approx 2000$ Pa) is considerably smaller than the conduction-driven value ($|p_1| = 2488$ Pa).

## 5. Concluding remarks

In this work, we theoretically examined a new mechanism of heat transfer in thermoacoustics, in which heat and mass are isothermally transferred between the working fluid and a sorbent boundary in the form of latent heat, rather than through conduction. Beginning with the conservation equations for a gas mixture in their most general form, we used an asymptotic expansion to de-couple the equations and simplify them into a set of ordinary differential equations. These equations were solved and manipulated into the form of a wave equation, and used to derive transport quantities, ultimately leading to the derivation of a differential equation for the axial temperature gradient imposed on the stack. The derived equations were subsequently used for a stability and limit cycle analyses. In the calculations we demonstrated how modifying a gas mixture to contain a reactive gas, able to exchange mass with a sorbent layer, decreases the temperature difference required to trigger an instability in thermoacoustic systems. These findings are in good agreement with experimental results obtained for an air–water mixture (Tsuda & Ueda 2017).

Onset temperature differences of various gas mixtures were compared, with the lowest values found for mixtures employing an inert component with a low heat capacity and reactive component with a low boiling temperature. Within our selection of gas mixtures, the air–MeOH mixture exhibited the lowest temperature difference required for onset of acoustic oscillations. Effects of gas mixture composition were investigated, revealing a clear dependency of the onset temperature difference on the reactive gas concentration $C_m$. As only the reactive gas is able to exchange phase with the sorbent boundary, increasing its fraction in the mixture enhances the effect, and hence decreases the onset temperature difference. A non-dimensional number, $\psi = (C_m/(1 - C_m))(l_h/RT_m)$, was found to be a good indicator for evaluating the performance of different sorbent/sorbate pairs, characterised by the sorbent/gas equilibrium curve shape, the latent heat released in the process and the gas mixture temperature.

The limit cycle analysis revealed that, with the addition of boundary mass exchange increasing $C_m$ significantly alters the wave form in the system, shifting it away from a standing-wave behaviour. The mass exchange within the stack results in recurrent injection/ejection of the reactive gas to/from the gas mixture, and thus intervenes with the natural tendency of the wave to resemble a standing wave. This wave-form

distortion increases the acoustic power in the system despite the decrease in pressure amplitude. Additionally, it also tends to decrease the resonant frequency as the travelling-wave component becomes dominant.

Effects of the reactive gas concentration, $C_m$, and the Womersley number, $\tau_v$ on a system's limit cycle temperature difference and pressure amplitude ($\Delta T$ and $|p_1|$) were examined. As expected, if $C_m$ is increased $\Delta T$ and $|p_1|$ decrease. The dependency on $\tau_v$ is far less trivial: the trend of $|p_1|$ versus $\tau_v$ at intermediate $\tau_v$ values may resemble a conduction-driven system, in which $|p_1|$ and $\Delta T$ minimise simultaneously since the pressure amplitude is proportional to the system thermal potential. However, at small or large $\tau_v$, as $\Delta T$ approaches its maximum value the wave form is greatly distorted, deviating from that of a standing wave. As a result, $|p_1|$ decreases as a system is forced to operate near its limiting $\tau_v$ values. At very large $C_m$, any resemblance to a conduction-driven system disappears and the phase-exchange system reveals a completely opposite trend – reaching a maximum for $\tau_v \approx 2$ and decreasing for small and large $\tau_v$.

Given a system sustaining a limit cycle, increasing the heat input $Q_h$ results in increased $|p_1|$ while $\Delta T$ remains constant. This non-intuitive result is explained by a simple analytic approximation, demonstrating how the proportionality $Q_h \propto |p_1|^2$, characterising standing-wave systems, yields a nearly constant temperature gradient in the stack.

Finally, we examined the effects of reaction kinetics on system stability as well as its limit cycle characteristics. The stability limit was calculated for various values of $K$, representing different sorbent affinities for the reactive component. Above a certain value of $K$, sorption kinetics result in monotonically increasing stability curves, displaying the lowest and highest temperature differences in the limit of fast and slow kinetics, respectively. A curious result is obtained for low values of $K$, in which the optimum for $\Delta T_{onset}$ is not in the limit of fast kinetics. Allowing partial relaxation for the desorbing gas in these cases proves to be beneficial, since the boundary affinity for sorption is highly limited. As opposed to the stability analysis, the limit of slow kinetics for a system limit cycle does not recover the conduction-driven result. Hydrodynamic dispersion of mass exists down the concentration gradient even if the oscillatory flow is induced by the conduction-driven mechanism. Moreover, a non-trivial minimum for $\Delta T$ is obtained even if ideal sorption is assumed ($K \to \infty$). A finite value of the dimensionless group $R_k/K \equiv \nu/(h^2 k_a)$ is found to minimise $\Delta T$ for practically any $K$ and $\tau_v$.

The results laid out in this work provide incentive for the use of phase-exchange thermoacoustics in the design of heat engines, capable of operating at low temperature differences and possibly produce higher acoustic power. As most low-grade heat sources are not sufficient for operation of commercially available heat engines, as well as conduction-driven thermoacoustic devices, phase-exchange thermoacoustic heat engines provide a promising alternative for exploiting these abundant heat sources.

**Acknowledgements**

The research was partially supported by grant 216-11-024 from the Israel Ministry of Energy and Water, and grant no. 345/13 from the Israel Science Foundation. The authors acknowledge the support from the Nancy and Stephen Grand Technion Energy Program (GTEP).

## Appendix A.

In what follows we show that the non-dimensional parameter $\psi$ is a monotonically decreasing function of the mean pressure. We begin by rewriting the definition

$$\psi = \frac{C_m}{1 - C_m} \frac{l_h}{RT_m}, \tag{A 1}$$

noting $\psi = f(C_m, l_h, T_m)$. Next, we expand $\mathrm{d}\psi/\mathrm{d}p_m$ as

$$\begin{aligned} \frac{\mathrm{d}\psi}{\mathrm{d}p_m} &= \left(\frac{\partial \psi}{\partial C_m}\right)_{l_h, T_m} \frac{\mathrm{d}C_m}{\mathrm{d}p_m} + \left(\frac{\partial \psi}{\partial l_h}\right)_{C_m, T_m} \frac{\mathrm{d}l_h}{\mathrm{d}p_m} + \left(\frac{\partial \psi}{\partial T_m}\right)_{C_m, l_h} \frac{\mathrm{d}T_m}{\mathrm{d}p_m} \\ &= \psi \left[\frac{1}{C_m(1 - C_m)} \frac{\mathrm{d}C_m}{\mathrm{d}p_m} + \frac{1}{l_h} \frac{\mathrm{d}l_h}{\mathrm{d}p_m} - \frac{1}{T_m} \frac{\mathrm{d}T_m}{\mathrm{d}p_m}\right]. \end{aligned} \tag{A 2}$$

For simplicity, we consider the case of phase change through evaporation/condensation, in which $C_m$ and $l_h$ are intuitively dependent on the mean pressure $p_m$. As $p_m$ is increased towards the critical pressure, the latent heat of evaporation decreases ($\mathrm{d}l_h/\mathrm{d}p_m < 0$) and the boiling temperature increases, such that $\mathrm{d}C_m/\mathrm{d}p_m < 0$. The temperature can only increases with pressure; hence, $\mathrm{d}T_m/\mathrm{d}p_m > 0$. All the terms multiplying the derivatives in (A 2) are positive. It is, therefore, clear that all three terms on the right-hand side of (A 2) are negative, and consequently $\mathrm{d}\psi/\mathrm{d}p_m < 0$.

## Appendix B.

Here, we describe the analytic approximation used in § 4.2.5 to show that extremum points in the temperature difference across the stack, $\Delta T$, at a given heating power, may only be obtained for a finite range of the Womersley number, $\tau_\nu$. The total power in a system is comprised of three fundamental elements: acoustic power, hydrodynamic dispersion and diffusion. Each of these terms appears twice in (2.65) – once for the conduction-driven and once for the phase-exchange mechanisms. In order to understand the effect of sorption kinetics, we only refer to the phase-exchange terms in (2.65); the typically weak effect of molecular diffusion on $\Delta T$ is neglected for the simplicity of this approximation. If a minimum of the heat converted to acoustic power is dispersed down the concentration (and temperature) gradient, $\Delta T$ is maximised. The converse of this statement is also correct: maximising the dispersion minimises $\Delta T$. We define a new variable, $\Sigma$, as the sum of phase-exchange acoustic power production and the (negative) heat flux due to hydrodynamic dispersion of the reactive component,

$$\Sigma = G_1 \mathrm{Re}\left[\frac{\widetilde{p_1} u_1}{\eta_D}\left(\frac{F_D - \widetilde{F_\nu}}{\widetilde{F_\nu}}\right)\right] - G_2 \mathrm{Im}\left[\widetilde{F_\nu}(1 + Sc) - \frac{\eta_\nu}{\eta_D}(\widetilde{F_\nu} - F_D)\right], \tag{B 1}$$

where $G_1$ and $G_2$ contain all the other physical variables in these two terms. The pressure and velocity may be expressed using the standing-wave approximation (§ 3.1.2) by (3.9)–(3.10), such that $\widetilde{p_1} u_1 \approx \mathrm{i} p_A^2 \sin(2x)/2$. For the sake of simplicity, as they serve merely as numerical pre-factors, we set $G_1 p_A^2 \sin(2x)/2 = G_2 = 1$, to obtain

$$\Sigma \approx -\left\{\mathrm{Im}\left[\frac{F_D - \widetilde{F_\nu}}{\eta_D \widetilde{F_\nu}}\right] + \mathrm{Im}\left[\widetilde{F_\nu}(1 + Sc) - \frac{\eta_\nu}{\eta_D}(\widetilde{F_\nu} - F_D)\right]\right\}. \tag{B 2}$$

We simplify the kinetics parameter, given explicitly in (2.47), by keeping only its dependence on $K$ and $R_k$ such that

$$\eta_n \approx 1 + \frac{1 - F_n}{K} + \mathrm{i}\frac{R_k}{K}(1 - F_n). \tag{B 3}$$

Further simplifying $\Sigma$, we consider the high frequency limit (also termed the 'boundary layer approximation' by Swift 1988), such that $F_\nu = 1 - \hat{\tau}_\nu^{-1}$ and $F_D = 1 - \hat{\tau}_\nu^{-1} Sc^{-1/2}$.

For the approximation presented in figure 9(*c*) we set $R_k \to 0$, such that $\eta_n \approx 1 + (1 - F_n)/K$. Setting $\mathrm{d}\Sigma/\mathrm{d}K = 0$ yields a quadratic equation for $K$, to which $K_{crit} = f(\tau_\nu, Sc)$, namely the critical partition coefficient for which a maximum in $\Delta T$ is obtained, is the solution. In one of the two solutions satisfying the equation, $K_{crit} < 0$ is obtained for all $\tau_\nu$ and $Sc$. In the second solution, however, positive values of $K_{crit}$ are obtained for a finite, intermediate range of $\tau_\nu$ regardless of the value assigned to $Sc$. This qualitative behaviour is sketched in the inset of figure 9(*c*) for $Sc = 0.6$, a representative value for an air–water vapour gas mixture.

The approximation presented in figure 9(*d*) is nearly identical to that of figure 9(*c*). Here we set $K \to \infty$, such that $\eta_n \approx 1 + \mathrm{i}(R_k/K)(1 - F_n)$, and derive a quadratic equation for $R_k/K$ by seeking the solution of $\mathrm{d}\Sigma/\mathrm{d}(R_k/K) = 0$. Again, only one of the solutions yields a physical result of $(R_k/K)_{crit} > 0$ for a finite range of $\tau_\nu$ and any positive $Sc$. A plot of $(R_k/K)_{crit}$ versus $\tau_\nu$ for $Sc = 0.6$ is sketched in the inset of figure 9(*d*).

## REFERENCES


Arnott, W. P., Bass, H. E. & Raspet, R. 1992 Specific acoustic impedance measurements of an air-filled thermoacoustic prime mover. *J. Acoust. Soc. Am.* **92** (6), 3432–3434.

Arnott, W. P., Belcher, J. R., Raspet, R. & Bass, H. E. 1994 Stability analysis of a helium-filled thermoacoustic engine. *J. Acoust. Soc. Am.* **96** (1), 370–375.

Bird, R. B., Stewart, W. E. & Lightfoot, E. N. 2007 *Transport Phenomena*, 2nd edn. Wiley.

Ceperley, P. H. 1979 A pistonless Stirling engine – the traveling wave heat engine. *J. Acoust. Soc. Am.* **66** (5), 1508–1513.

Dowling, A. P. & Morgans, A. S. 2005 Feedback control of combustion oscillations. *Annu. Rev. Fluid Mech.* **37** (1), 151–182.

Fleifil, M., Annaswamy, A. M., Ghoneim, Z. A. & Ghoniem, A. F. 1996 Response of a laminar premixed flame to flow oscillations: a kinematic model and thermoacoustic instability results. *Combust. Flame* **106** (4), 487–510.

Hiller, R. A. & Swift, G. W. 2000 Condensation in a steady-flow thermoacoustic refrigerator. *J. Acoust. Soc. Am.* **108** (4), 1521–1527.

Keller, J. J. 1995 Thermoacoustic oscillations in combustion chambers of gas turbines. *AIAA J.* **33** (12), 2280–2287.

Landau, L. D. & Lifshitz, E. M. 1959 *Fluid Mechanics*. Pergamon.

Majer, V. & Svoboda, V. 1985 *Enthalpies of Vaporization of Organic Compounds: A Critical Review and Data Compilation*. Blackwell Scientific.

Meir, A., Offner, A. & Ramon, G. Z. 2018 Low-temperature energy conversion using a phase-change acoustic heat engine. *Applied Energy* **231**, 372–379.

Noda, D. & Ueda, Y. 2013 A thermoacoustic oscillator powered by vaporized water and ethanol. *Am. J. Phys.* **81** (2), 124–126.

Poling, B. E., Prausnitz, J. M. & O'Connell, J. P. 2001 *The Properties of Gases and Liquids*. McGraw-Hill.

RASPET, R., SLATON, W. V., HICKEY, C. J. & HILLER, R. A. 2002 Theory of inert gas-condensing vapor thermoacoustics: propgation equations. *J. Acoust. Soc. Am.* **112** (4), 1414–1422.

RIJKE, P. L. 1859 Notiz über eine neue Art, die in einer an beiden Enden offenen Röhre enthaltene Luft in Schwingungen zu versetzen. *Ann. Phys.* **183** (6), 339–343.

ROTT, N. 1969 Damped and thermally driven acoustic oscillations in wide and narrow tubes. *Z. Angew. Math. Phys.* **20** (2), 230–243.

SLATON, W. V., RASPET, R., HICKEY, C. J. & HILLER, R. A. 2002 Theory of inert gas-condensing vapor thermoacoustics: transport equations. *J. Acoust. Soc. Am.* **112** (4), 1423–1430.

SONDHAUSS, C. 1850 Ueber die Schallschwingungen der Luft in erhitzten Glasröhren und in gedeckten Pfeifen von ungleicher Weite. *Ann. Phys.* **155** (1), 1–34.

SWIFT, G. W. 1988 Thermoacoustic engines. *J. Acoust. Soc. Am.* **84** (4), 1145–1180.

SWIFT, G. W. 1992 Analysis and performance of a large thermoacoustic engine. *J. Acoust. Soc. Am.* **92** (3), 1551–1563.

SWIFT, G. W. 2002 *Thermoacoustics: A Unifying Perspective for Some Engines and Refrigerators*. Acoustic Society of America.

TSUDA, K. & UEDA, Y. 2015 Abrupt reduction of the critical temperature difference of a thermoacoustic engine by adding water. *AIP Adv.* **5** (9), 097173.

TSUDA, K. & UEDA, Y. 2017 Critical temperature of traveling- and standing-wave thermoacoustic engines using a wet regenerator. *Appl. Energy* **196**, 62–67.

WARD, W. C. & SWIFT, G. W. 1994 Design environment for low amplitude thermoacoustic engines. *J. Acoust. Soc. Am.* **95** (6), 3671–3672.

WELTSCH, O., OFFNER, A., LIBERZON, D. & RAMON, G. Z. 2017 Adsorption-mediated mass streaming in a standing acoustic wave. *Phys. Rev. Lett.* **118** (24), 244301.

YAZAKI, T., IWATA, A., MAEKAWA, T. & TOMINAGA, A. 1998 Traveling wave thermoacoustic engine in a looped tube. *Phys. Rev. Lett.* **81** (15), 3128–3131.